Aalto University
School of Science
Degree Programme in Engineering Physics and Mathematics

Ville Vierimaa

# Spin-Dependent transport in Graphene

Master's Thesis

Espoo, March 14, 2016

Supervisor: D.Sc. Ari Harju

Thesis advisor(s): D.Sc. Ari Harju

Aalto University
School of Science

**Abstract of master's thesis**

**Author:** Ville Vierimaa

**Title of thesis:** Spin-Dependent transport properties of Graphene

**Master's programme:** Degree Programme in Engineering Physics and Mathematics

**Thesis supervisor:** D.Sc. Ari Harju

**Major or Minor/Code:** Engineering Physics (F3005)

**Department:** Department of Applied Physics

**Thesis advisor(s):** D.Sc. Ari Harju

| Date | Number of pages | Language |
|---|---|---|
| 14.3.2016 | 47 | English |

**Abstract**

Graphene is a 2-dimensional allotrope of carbon which has attracted a lot of interest since its discovery in 2004. It has high electron mobility and small intrinsic spin-orbit-coupling, leading to long spin persistence lengths. This makes it an interesting material for spintronics as it can be used as a platform for spin-dependent defects. Its spin behaviour is almost completely determined by the defects, which can be used to tune its properties.

The electronic transport properties of graphene are most commonly studied by Landauer-Büttiker and Kubo-Greenwood methods. They both work well with the tight-binding model, which recovers the electronic band structure of graphene correctly, and they give results consistent with each other. The difference between the two is that Landauer-Büttiker is more suitable for narrow ribbons, while Kubo-Greenwood performs better in wider systems.

In this thesis, a spinful version of the Kubo-Greenwood method is derived and then implemented on top of an existing spinless version. The implementation is done with Nvidia CUDA and it runs on graphics processing units. Different spin-dependent defects in graphene are used to test the implementation and validate the method.

While the spinful version of the method is easy to implement, it turns out that it lacks the ability to completely describe spin-flipping current. Spin-conserving conductivity is given correctly by the method and spin polarization is proposed to describe the spin behavior better. Long-ranged scatterers are found to scatter spin more efficiently than they do charge and they are suggested to be partly responsible for the experimentally found short spin relaxation times.

**Keywords** graphene, spin, Kubo-Greenwood, CUDA, GPU

Aalto-yliopisto
Perustieteiden
korkeakoulu

**Diplomityön tiivistelmä**

**Tekijä:** Ville Vierimaa

**Työn nimi:** Grafeenin spin-riippuva johtavuus

**Koulutusohjelma:** Teknillinen fysiikka ja matematiikka

**Valvoja:** TkT Ari Harju

**Pää tai sivuaine/koodi:** Teknillinen fysiikka (F3005)

**Työn ohjaaja(t):** TkT Ari Harju

**Päivämäärä** 14.3.2016 **Sivumäärä** 47 **Kieli** Englanti

**Tiivistelmä**

Grafeeni on hiilen kaksiulotteinen allotrooppi, joka löydettiin vuonna 2004. Sen elektroneilla on suuri liikkuvuus ja pieni spin–rata-kytkentä, jonka ansiosta spinin relaksaatiopituus kasvaa huomattavan suureksi. Grafeeni on erityisen kiinnostava materiaali spintroniikassa, jossa sitä voidaan käyttää alustana spin-riippuville epäpuhtauksille. Sen spinin ominaisuudet ovat lähes täysin epäpuhtauksien määrittelemät, joten spin käytöstä voidaan säätää niiden avulla.

Grafeenin johtavuusominaisuuksia tutkitaan yleensä joko Landauer-Büttiker- tai Kubo-Greenwood-menetelmillä. Molemmat toimivat hyvin tiukan sidoksen mallin kanssa ja antavat keskenään vertailukelpoisia tuloksia. Menetelmien erona ovat systeemit, joihin ne soveltuvat. Landauer-Büttiker toimii paremmin kapeammissa nauhoissa, kun taas Kubo-Greenwood soveltuu hyvin leveämpiin, täysin kaksiulotteisiin systeemeihin.

Tässä työssä johdetaan spinillinen versio Kubo-Greenwood-menetelmästä ja toteutetaan se aikaisemman spinittömän version pohjalta. Toteutus tehdään Nvidian CUDA-kielellä ja sitä voidaan ajaa näytönohjaimilla. Toteutusta testataan erilaisilla spin-riippuvilla epäpuhtausmalleilla.

Spinillinen versio on helposti johdettavissa spinittömästä versiosta, mutta käy ilmi, ettei se kuvaa täysin spinien välistä virtaa. Menetelmä antaa kuitenkin oikein spinin säilyttävän konduktiivisuuden ja spinin polarisaatio osoittautuu paremmaksi ominaisuudeksi kuvaamaan spinin käytöstä. Tutkituista epäpuhtauksista pitkän matkan sirottajat sirottivat spiniä suhteessa varaukseen eniten ja niitä ehdotetaan osatekijäksi kokeissa havaittuihin lyhyisiin relaksaatiopituuksiin.

**Avainsanat** grafeeni, spin, Kubo-Greenwood, GPU

# Contents

# 1 Introduction

Spintronics is an emerging branch of electronics which has gained much attention over the past few decades. It utilizes the spin degree of freedom of the electrons, which enables a much wider range of components and devices [1, 2]. Since there are two kinds of currents, up and down polarized, it is in principle possible to design a component that reacts in one way to up current and in another to down current. This is relevant, for example, in logic and memory components, which can benefit from having a second degree of freedom or even use the spin as their only state indicator [3]. A good example of this is the giant magnetoresistance effect (GMR) used in magnetic memories, which is based on the magnetic alignment of ferromagnetic films [4].

Spin is an intrinsic property of electrons, similar to charge or mass. It is a relativistic effect arising from the Dirac equation resembling angular momentum and most importantly, it serves as a source of magnetic moment for electrons. In ferromagnetic materials the alignment of the moments is energetically favoured and there is a net spin polarization. When the net moment of a material is non-zero, magnetic properties can be observed even macroscopically.

Instead of having the whole material made of magnetic atoms, it is possible to have mostly non-magnetic material with some magnetic defects in it [5, 6]. This offers an interesting system to study, since even a small amount of defects can make spin-dependent behaviour arise[7, 8]. This work mostly focuses on the spin polarization and conductivity of graphene with magnetic defects in it. Graphene provides an appealing platform for magnetic defects because it has small intrinsic spin-orbit coupling (SOC) [9, 10], which means the spin-behaviour is almost completely dictated by the defects in the system. Graphene also possesses high electronical conductivity and low scattering rates, making it a promising material for spintronics [11, 12].

The two main methods to model the electronic transport properties of graphene are the Kubo-Greenwood (KG) [13, 14] and Landauer-Büttiker (LB)[15] formalisms. In this work the focus is mostly on the Kubo-Greenwood, even though some comparisons will be done between the two methods. Both of the methods work within the tight-binding model [16], which describes the electronic properties of graphene relatively well. It predicts the band structure correctly near the zero energy and is not too bad either at higher energies [17]. Because of its simple format, it serves as a good starting point also for modelling defects in graphene. Taking spin into account in the model is not hard either [18], which makes it ideal for our uses.

When spin-dependent defects are modelled, the orientation of their spin axis plays an important role. If polarized current interacts with defect which is aligned parallel or anti-parallel with the polarization, the current retains its polarization. The defect will have separate properties for both polarizations, but there will be no connection between the spin channels. The situation becomes much more interesting when the defect axis is not aligned with the polarization. This allows spin to flip at the defect sites and makes the system

much more complicated, as it can no longer be modelled as two separate non-interacting subsystems.

In addition to the defect alignment, the location of the defects relative to each other has a major effect on the properties, especially in graphene [19]. Graphene consists of two sublattices and depending on whether two defects are on the same one or not will impact the properties greatly in some cases [20, 21]. Because there are a lot of parameters regarding the defects, it may be hard to get a good overview of the average properties of certain defects. Some interesting properties may be present only in a certain configuration and some may only appear in highly randomized systems. Therefore, to get a good conclusion on what properties certain defects would have in a real world experiment, the averaging of the defect properties should be done well. One way of doing this is to simulate larger systems.

One downside of big simulations is the increased computational effort. In the best case scenario, the computational time will increase linearly with respect to the number of atoms, but even linear scaling can take one only so far on its own. In practise, all large scale simulations require some kind of parallelization to make the simulation run in reasonable time. Parallelization can be done on the CPU, on which it is also relatively easy to implement. However, a good alternative to CPU implementation is the use of graphics processing units (GPUs). The GPUs have a vast amount of computational power inside and when the implementation is done correctly, they can reach impressive speedups over regular CPUs [22, 23].

There are some limitations to the use of GPUs, however. Their architecture is much simpler compared to CPUs and they require a bit different approach [24]. One of the most important factors in the choice between CPU and GPU is the arithmetic intensity of the calculation being implemented [25]. It is determined by the ratio between arithmetic operations and the memory accesses and the higher it is, the better the GPUs relative performance will be. This is because the internal memory GPUs have is slow and transferring data to the GPU from the CPU memory is even slower [26]. Doing every single calculation on the GPU is usually not an option either because they perform quite poorly in executing sequential code. Getting the best performance usually requires careful analysis to identify the parts which benefit most from being calculated on the GPU [27, 28].

The goal of this thesis is to derive and implement spinful version of the Kubo-Greenwood method, starting from an existing spinless implementation [29] and test it on various spin-dependent defects. The method is linear-scaling and it works really well even for larger systems, as required. The original code is written in CUDA C [30] and is optimized to run on GPUs. The new implementation will also be written in CUDA. The focus in the calculations will be on the conductivity and spin polarization of graphene with different kinds of spin-dependent potentials, but some attention is also given to graphene nanoribbons and alternative defect models.

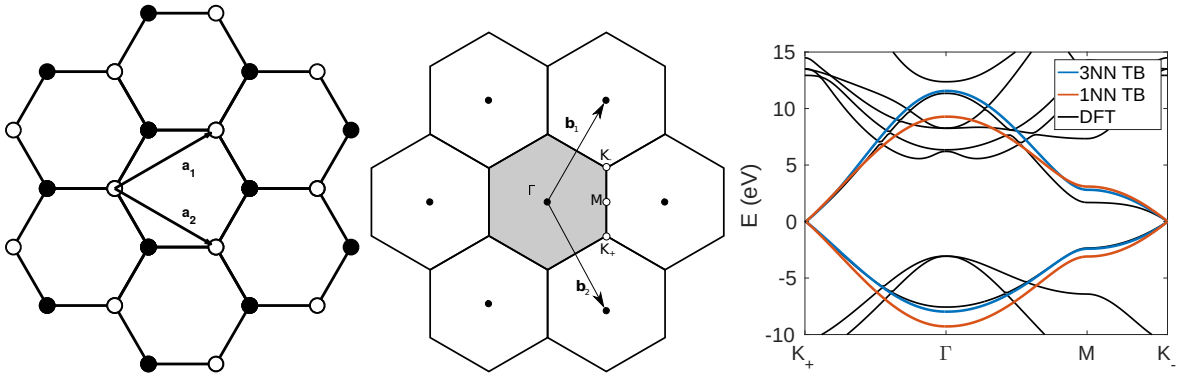


(a) (b) (c)

Figure 1: (a) Real-space (b) Reciprocal lattices of graphene. Vectors $a$ and $b$ show the basis vectors for both lattices. (c) Band structure of graphene calculated with TB and DFT.

## 2 Tight-binding model for spin-dependent defects

The carbon atoms in graphene are arranged in a honeycomb lattice as show in Fig. 1a. The atoms are $sp^2$-hybridized, which means that three of the four valence electrons of each atom are used to form $\sigma$-bonds between neighbours and the fourth one is left to form a $p_z$-type orbital. Because the $\sigma$-bonds are strong and have a low energy, all of the effects near the Fermi level are caused by the $p_z$-electrons. This justifies the use of the tight-binding model, for which the basis functions are localized at each atom site. The hopping $t_{ij} = \langle\psi_i|\hat{H}|\psi_j\rangle$ between these basis functions determines the coupling between each pair of atoms. It is usually sufficient to consider only a few of the nearest sites for each atom, because the hoppings to further atoms go to zero relatively fast.

In graphene, the hoppings are usually taken up to the first or the third nearest neighbours. The first neighbours description is valid near the Fermi level, but it becomes less accurate further in energy [31]. The band structure given by the 1st neighbour description is completely symmetric in energy, a fact that is not supported by the *ab initio* calculations, as shown by Fig. 1c. The 3rd neighbours however can recover this behaviour and give a much more accurate description of the bands [32]. The drawback is that it is more complicated to implement and the calculations take a lot longer. In our case we are more interested in the behaviour of the defects and the 1st neighbour description is enough for our needs.

For pristine graphene, the 1st neighbour tight binding Hamiltonian reads

$$\hat{H}_0 = t_0 \sum_{\langle i,j\rangle} |i\rangle\langle j|, \tag{1}$$

where the sum goes over pairs of neighbours $\langle i,j\rangle$. The pristine Hamiltonian can be used as a starting point when we add defects to the system by writing the total Hamiltonian as a sum of $\hat{H}_0$ and the defect Hamiltonian $\hat{H}_d$:

$$\hat{H} = \hat{H}_0 + \hat{H}_d. \tag{2}$$

The defect Hamiltonian can either modify the hoppings or add a local potential. In either case, we need to consider the alignment of the defects' spin axis. The axis lies somewhere on the Bloch sphere and in a general case can be different for different defect sites. Depending on the type of the defects, there could be some correlation between the defect axes but at least in the dilute limit in the absence of magnetic field, there should not be magnetic ordering between the defects.

The defect Hamiltonian for a single site with spin dependent potential can be written as

$$\hat{H}_d = |i\rangle\langle i| \otimes (U_\uparrow |\uparrow\rangle\langle\uparrow| + U_\downarrow |\downarrow\rangle\langle\downarrow|), \tag{3}$$

where $i$ is the index of the site and $U_{\uparrow,\downarrow}$ are the potentials for each spin [18]. We choose the sample z-axis to be the reference direction and rotate the spin vectors to this basis. To do this, the defect Hamiltonian is written in terms of the average and difference of the potentials:

$$\hat{H}_d = |i\rangle\langle i| \otimes \left( \frac{U_\uparrow + U_\downarrow}{2} I + \frac{U_\uparrow - U_\downarrow}{2} \sigma_z^d \right), \tag{4}$$

where $\sigma_z^d$ is the Pauli z-matrix in the defect basis [33]. Rotation only applies to $\sigma_z^d$, which transforms into

$$\sigma_z^d = \begin{bmatrix} \cos(\theta) & e^{-i\phi}\sin(\theta) \\ e^{i\phi}\sin(\theta) & -\cos(\theta) \end{bmatrix} \tag{5}$$

where angles $\theta$ and $\phi$ refer to location of the defect on the Bloch sphere. In case of multiple defects, the Hamiltonian is acquired by summing over all of the defect sites.

Defects with spin dependent hoppings can be modelled almost identically to the potential defects. Similar to potential defects, we assume that each spin has its own hopping strength to the defect atom, denoted by $t_\uparrow$ and $t_\downarrow$. The only difference to Eq. 3 comes from the fact that a single defect site has multiple hoppings. To get the complete defect Hamiltonian for single site, we need to sum over all of the hoppings to and from the defect site:

$$\hat{H}_d = \sum_{\langle i,j\rangle \in d} |i\rangle\langle j| \otimes (t_\uparrow |\uparrow\rangle\langle\uparrow| + t_\downarrow |\downarrow\rangle\langle\downarrow|). \tag{6}$$

In the case of graphene considering only the nearest neighbours, there are 6 terms in this sum. The same changes can also be made to Eq. 4 to apply the spin rotation to the defect.

Because potential and hoppings are the only parameters in the tight-binding model, these two defect types can be combined to model any defect reachable by tight-binding. Defects that are not localized on atom sites may need different summations than Equations 3 and 6, but the main idea remains the same. The defects modellable by this method range from simple mathematical defects where potential or hoppings are changed for a chosen number of sites to complex multi-site defects originating from physical observations.

# 3 Methods

## 3.1 Landauer-Büttiker formalism

The setting in the Landauer theory is to consider a sample or device connected to reservoirs through leads. Conductance is seen as a scattering process, in which electrons are injected through one lead to the device, from which they are scattered back to the reservoirs. The method was generalized to multiple leads by Büttiker [34] and the current between leads $i$ and $j$ can be written as

$$I_{i,j} = \frac{2e}{h} \int T_{j,i} f_i(\epsilon) - T_{i,j} f_j(\epsilon) d\epsilon, \tag{7}$$

where $T_{i,j}$ is the transmission function or transmittance between the leads and $f_i(\epsilon)$ is the Fermi function for the corresponding reservoir [35]. The Fermi functions in the equation implicitly include the effect of the chemical potential in each of the leads, which complicates the calculation. However, most of the times it is enough to focus entirely on the transmission functions of the device, since they don't depend on the chemical potential. Additionally, they gives an access to the transport properties of the device, since conductivity is directly proportional to it.

For pristine graphene, the calculation of the transmission function is easy, since there is no scattering occurring and the transmittance only depends on the number of transport modes. The number of modes is determined by the band structure and transmittance is trivial to calculate once the band structure is known. However, in the presence of defects the calculation is not as easy any more as scattering occurs in the device area. An efficient way of accessing the transmittance is through the Green's function, defined as [36]

$$G(EI - H) = I. \tag{8}$$

The use of the tight-binding basis makes the Green's function discrete, making it rather easy to calculate. There is a slight problem with the problem dimension, since the leads need to be considered semi-infinite, making the matrix dimension in Eq. 8 infinite, but recursive calculation can be used to summarize the effect of each lead into simple finite-sized matrices $\Sigma$ called self-energies of the leads [37]. After writing the Eq. 8 in block form, it is possible to solve for the part of the Green's function $G_D$, which corresponds to the device area:

$$G_D = \left(EI - H_D - \Sigma_L - \Sigma_R\right)^{-1}, \tag{9}$$

with $H_D$ being the Hamiltonian of the device area.

Once the Green's functions and self energies have been calculated, it's possible to proceed to calculating the transmittance. By considering the scattering in the device, it's possible to show that transmittance from one lead to another can be written as [15]:

$$T_{i,j} = \mathrm{Tr}\left[\Gamma_i G_D \Gamma_j G_D^\dagger\right], \tag{10}$$

where $\Gamma_i$ is a function describing the coupling of lead $j$ to the device and is defined as

$$\Gamma_j = i\left[\Sigma_j - \Sigma_j^\dagger\right]. \tag{11}$$

The spin-dependent properties are easy to calculate from Eq. 10. Instead of considering a regular two-terminal setup where we inject current from one side of the device and measure from the other, it is possible to use a four-terminal setup in which each of the two leads are replaced by two spin-polarized leads. Injection of spin-polarized current can then be thought as current from one lead to the other three, allowing the calculation of spin-conserving and spin-flipping transmittances.

## 3.2 Spin-dependent conductivity

The Kubo conductivity for a system with eigenstates $|n\rangle$ can be written as

$$\sigma(\omega) = \frac{\pi\hbar e^2}{\Omega}\sum_{m,n}|\langle m|\hat{V}_x|n\rangle|^2\delta(E_m - E_n - \hbar\omega)\frac{f(E_n) - f(E_m)}{\hbar\omega}, \tag{12}$$

where $E_n$ is the (eigen)energy of state $n$, $\hat{V}_x$ is the velocity operator and $f(E)$ is the Fermi function [35]. States $|m\rangle$ and $|n\rangle$ correspond to initial and final states of the system. We can study the current from one spin channel to another by projecting these states to the initial and final spin channels. This can be done with spin filter operators $\hat{\sigma}_\uparrow$ and $\hat{\sigma}_\downarrow$, which behave as identity for one spin and as a zero for the other.

Denoting the initial spin by $\sigma_1$ and the final spin by $\sigma_2$, the conductance between these two can be written as:

$$\sigma(\omega)^{\sigma_1\to\sigma_2} = \frac{\pi\hbar e^2}{\Omega}\sum_{m,n}\langle m|\hat{\sigma}_1\hat{V}_x^\dagger\hat{\sigma}_2|n\rangle\langle n|\hat{\sigma}_2\hat{V}_x\hat{\sigma}_1|m\rangle\delta(E_m - E_n - \hbar\omega)\frac{f(E_n) - f(E_m)}{\hbar\omega}. \tag{13}$$

Instead of applying the operators $\hat{\sigma}$ to the state vectors, we can apply them to $\hat{V}_x$, defining us a new operator $\hat{V}_{\hat{\sigma}} = \hat{\sigma}_2\hat{V}_x\hat{\sigma}_1$. Also, the functions outside of the inner product don't have operators in them, allowing us to move them inside:

$$\sigma(\omega)^{\sigma_1\to\sigma_2} = \frac{\pi\hbar e^2}{\Omega}\sum_{m,n}\langle m|\hat{V}_{\hat{\sigma}}^\dagger|n\rangle\langle n|\hat{V}_{\hat{\sigma}}\frac{f(E_n) - f(E_m)}{\hbar\omega}\delta(E_m - E_n - \hbar\omega)|m\rangle. \tag{14}$$

The energy difference between $|m\rangle$ and $|n\rangle$ is equal to $\hbar\omega$, which means we can replace $E_m$ inside the Fermi function with $E_n + \hbar\omega$. On the other hand, $E_m$ is the eigenenergy of $|m\rangle$ and the relation $\hat{H}|m\rangle = E_m|m\rangle$ can be used to replace $E_m$ inside the delta function with $\hat{H}$. Also, $\delta(x) = \delta(-x)$, giving us:

$$\sigma(\omega)^{\sigma_1\to\sigma_2} = \frac{\pi\hbar e^2}{\Omega}\sum_{m,n}\langle m|\hat{V}_{\hat{\sigma}}^\dagger|n\rangle\langle n|\hat{V}_{\hat{\sigma}}F(E_n)\delta(E_n + \hbar\omega - \hat{H})|m\rangle, \tag{15}$$

where $\frac{f(E_n)-f(E_n+\hbar\omega)}{\hbar\omega}$ has been replaced with $F(E_n)$ to shorten the notation. To get rid of $E_n$, another delta function can be brought inside the summation using the property $\int \delta(x-a)f(x)dx = f(a)$:

$$\sigma(\omega)^{\sigma_1\to\sigma_2} = \frac{\pi\hbar e^2}{\Omega}\sum_{m,n}\int dE\delta(E-E_n)\langle m|\hat{V}_{\hat{\sigma}}^{\dagger}|n\rangle\langle n|\hat{V}_{\hat{\sigma}}F(E)\delta(E+\hbar\omega-\hat{H})|m\rangle. \tag{16}$$

Similar to what was done earlier, the delta function can be taken inside the inner product and $E_n$ can be replaced with the Hamiltonian. This way the only references to $m$ and $n$ inside the summation are in the states, allowing us to re-order our expression:

$$\sigma(\omega)^{\sigma_1\to\sigma_2} = \frac{\pi\hbar e^2}{\Omega}\int dEF(E)\sum_{m,n}\langle m|\hat{V}_{\hat{\sigma}}^{\dagger}\delta(E-\hat{H})\left(|n\rangle\langle n|\right)\hat{V}_{\hat{\sigma}}\delta(E+\hbar\omega-\hat{H})|m\rangle. \tag{17}$$

Because the vectors $|n\rangle$ form a complete orthonormal basis, $\sum_n |n\rangle\langle n| = I$. Likewise, we can identify $\sum_m \langle m|\hat{A}|m\rangle$ to be equal to $\mathrm{Tr}\hat{A}$, giving us

$$\sigma(\omega)^{\sigma_1\to\sigma_2} = \frac{\pi\hbar e^2}{\Omega}\int dEF(E)\mathrm{Tr}\left\{\hat{V}_{\hat{\sigma}}^{\dagger}\delta(E-\hat{H})\hat{V}_{\hat{\sigma}}\delta(E+\hbar\omega-\hat{H})\right\}. \tag{18}$$

For DC current at zero temperature, the equation simplifies to

$$\sigma(E)^{\sigma_1\to\sigma_2} = \frac{\pi\hbar e^2}{\Omega}\mathrm{Tr}\left\{\hat{V}_{\hat{\sigma}}^{\dagger}\delta(E-\hat{H})\hat{V}_{\hat{\sigma}}\delta(E-\hat{H})\right\}. \tag{19}$$

One of the delta functions can be written as a Fourier transform:

$$\delta(E-\hat{H}) = \frac{1}{2\pi\hbar}\int_{-\infty}^{\infty}\mathrm{d}te^{i(E-\hat{H})t/\hbar}. \tag{20}$$

Because $e^{iEt/\hbar}$ is just a number, we can move it freely. However, the second delta function allows us to replace $E$ with $\hat{H}$, giving us

$$\sigma(E)^{\sigma_1\to\sigma_2} = \frac{e^2}{2\Omega}\int_{-\infty}^{\infty}\mathrm{d}t\mathrm{Tr}\left\{U^{\dagger}\hat{V}_{\hat{\sigma}}^{\dagger}U\hat{V}_{\hat{\sigma}}\delta(E-\hat{H})\right\}, \tag{21}$$

where we have introduced the time evolution operator $U = e^{-i\hat{H}t/\hbar}$. Splitting the integral into two parts and changing variable $t \leftarrow -t$ for one of them allows us to write this as

$$\sigma(E)^{\sigma_1\to\sigma_2} = \frac{e^2}{\Omega}\int_0^{\infty}\mathrm{d}t\mathrm{Tr}\left\{\frac{\hat{V}_{\hat{\sigma}}^{\dagger}(t)\hat{V}_{\hat{\sigma}}+\hat{V}_{\hat{\sigma}}^{\dagger}\hat{V}_{\hat{\sigma}}(t)}{2}\delta(E-\hat{H})\right\}. \tag{22}$$

The function we are taking the integral over can be recognized as the real part of the autocorrelation function of our spin velocity operator, defined as

$$C_{vv}(E,t) = \frac{\mathrm{Tr}\left\{\frac{1}{\Omega}\hat{V}_{\hat{\sigma}}^{\dagger}(t)\hat{V}_{\hat{\sigma}}\delta(E-\hat{H})\right\}}{\mathrm{Tr}\left\{\frac{1}{\Omega}\delta(E-\hat{H})\right\}}, \tag{23}$$

multiplied by the density of states

$$\rho(E) = \mathrm{Tr}\left\{\frac{1}{\Omega}\delta(E-\hat{H})\right\}. \tag{24}$$

### 3.3 Comparison between spinful and spinless cases

For the spinless case, we will get an almost identical formula for conductivity. The only differences are that we do not include the spin-filtering operators in the beginning and spin-degeneracy gives a factor of 2 in front of the equation. Without the filters, we are left with regular velocity operators. Also, from a practical point of view, it is better to calculate the running electrical conductivity (REC) instead of taking the limit of time going to infinity:

$$\sigma(E,t)^{GK} = \frac{2e^2}{\Omega}\int_0^t \mathrm{dt}\ \mathrm{Tr}\left\{\frac{\hat{V}^\dagger(t)\hat{V} + \hat{V}^\dagger\hat{V}(t)}{2}\delta(E-\hat{H})\right\}. \tag{25}$$

The equation above is called Green-Kubo formula because it gives the conductivity as an integral of velocity autocorrelation function [38]. As with other Green-Kubo formulas, a corresponding Einstein formula can be found by applying an integral. In this case, the derivative of mean squared displacement (MSD), defined as

$$\Delta X^2(E,t) = \frac{\mathrm{Tr}\left[\frac{2}{\Omega}\delta(E-\hat{H})(\hat{X}(t)-\hat{X})^2\right]}{\mathrm{Tr}\left[\frac{2}{\Omega}\delta(E-\hat{H})\right]}, \tag{26}$$

is found to give the conductivity:

$$\sigma(E,t)^E = e^2\rho(E)\frac{\mathrm{d}}{2\mathrm{dt}}\Delta X^2(E,t). \tag{27}$$

Calculating the conductivity from the Einstein relation is more accurate because differentiation does not accumulate error in the same way integration does. Therefore longer time steps can be used, as the length now only affects the accuracy of time evolution. However, in the more interesting spinful case, a similar relation can only be found when there is no coupling between the spins.

The case with no coupling between the spins can be reduced to two spinless calculations, so we assume for now that there is coupling between the spins, that is $\hat{H}_{\uparrow\downarrow}$ and $\hat{H}_{\downarrow\uparrow}$ are non-zero. If the conductivity should be a derivative of some operator $\tilde{X}$ squared, that operator would have to be defined as

$$\tilde{X}(t) = \int_0^t \hat{V}_\sigma(t')\mathrm{dt}' + \tilde{X}(0) \tag{28}$$

to give conductivity consistent with Eq. 22. If this equation in differentiated, we will have

$$\frac{\mathrm{d}}{\mathrm{dx}}\tilde{X}(t) = \hat{V}_\sigma(t). \tag{29}$$

The right hand side of the equation is known:

$$\begin{aligned}\hat{V}_\sigma(t) &= \hat{U}^\dagger \sigma_2 \hat{V}_x \sigma_1 \hat{U} \\ &= \hat{U}^\dagger \sigma_2 [H, X] \sigma_1 \hat{U}.\end{aligned} \tag{30}$$

On the other side, we can write the derivative of $\tilde{X}$ as a commutator:

$$\frac{\mathrm{d}}{\mathrm{dx}} \tilde{X}(t) = \hat{U}^\dagger [H, \tilde{X}] \hat{U}. \tag{31}$$

Comparing these two equations, we require $\tilde{X}$ to fulfil the relation

$$[H, \tilde{X}] = \hat{\sigma}_2 [H, X] \hat{\sigma}_1. \tag{32}$$

Let us consider the commutator of $\hat{H}$ with arbitrary operator $\hat{O}$. Both of the operators can be written in block form: $\hat{H} = \begin{bmatrix} H_{\uparrow\uparrow} & H_{\uparrow\downarrow} \\ H_{\downarrow\uparrow} & H_{\downarrow\downarrow} \end{bmatrix}$ and $\hat{O} = \begin{bmatrix} A & B \\ C & D \end{bmatrix}$. In terms of these blocks, the commutator becomes:

$$[\hat{H}, \hat{O}] = \begin{bmatrix} [H_{\uparrow\uparrow}, A] + H_{\uparrow\downarrow} C - B H_{\downarrow\uparrow} & H_{\uparrow\uparrow} B + H_{\uparrow\downarrow} D - A H_{\uparrow\downarrow} - B H_{\downarrow\downarrow} \\ H_{\downarrow\uparrow} A + H_{\downarrow\downarrow} C - C H_{\uparrow\uparrow} - D H_{\downarrow\uparrow} & [H_{\downarrow\downarrow}, D] + H_{\downarrow\uparrow} B - C H_{\uparrow\downarrow} \end{bmatrix}. \tag{33}$$

The left hand side of Eq. 32 will have exactly the same form as this equation, while the right hand side will become

$$\hat{\sigma}_2 [H, X] \hat{\sigma}_1 = \begin{bmatrix} [H_{\uparrow\uparrow}, X] + H_{\uparrow\downarrow} X - X H_{\downarrow\uparrow} & 0 \\ 0 & 0 \end{bmatrix}, \tag{34}$$

assuming $\sigma_1 = \sigma_2 = \sigma_\uparrow$. If we want $\tilde{X}$ to be same regardless of the system, it should not depend on the Hamiltonian. Also, it is possible to change diagonal blocks of the Hamiltonian without altering the off-diagonal part. These two conditions allow us to separate the terms containing diagonal and off-diagonal parts of the Hamiltonian, handling them as their own equations. If we now compare the diagonal blocks of Eq. 32, we will have

$$[H_{\uparrow\uparrow}, \tilde{X}_{\uparrow\uparrow}] + H_{\uparrow\downarrow} \tilde{X}_{\downarrow\uparrow} - \tilde{X}_{\uparrow\downarrow} H_{\downarrow\uparrow} = [H_{\uparrow\uparrow}, X] + H_{\uparrow\downarrow} X - X H_{\downarrow\uparrow} \tag{35}$$

and

$$[H_{\downarrow\downarrow}, \tilde{X}_{\downarrow\downarrow}] + H_{\downarrow\uparrow} \tilde{X}_{\uparrow\downarrow} - \tilde{X}_{\downarrow\uparrow} H_{\uparrow\downarrow} = 0. \tag{36}$$

The diagonal part of the first equation gives us $[H_{\uparrow\uparrow}, \tilde{X}_{\uparrow\uparrow}] = [H_{\uparrow\uparrow}, X]$ and the second equation gives us $[H_{\downarrow\downarrow}, \tilde{X}_{\downarrow\downarrow}] = 0$. If these conditions hold for any Hamiltonian, the only solution is $\tilde{X}_{\uparrow\uparrow} = X$, $\tilde{X}_{\downarrow\downarrow} = 0$.

More conditions for $\tilde{X}$ can be found from the off-diagonal blocks of Eq. 32. The off-diagonal parts of the Hamiltonian give us equation

$$H_{\uparrow\downarrow} \tilde{X}_{\downarrow\downarrow} - \tilde{X}_{\uparrow\uparrow} H_{\uparrow\downarrow} = 0. \tag{37}$$

However, we concluded that $\tilde{X}_{\downarrow\downarrow} = 0$, which means that $\tilde{X}_{\uparrow\uparrow}$ should be zero as $\hat{H}_{\uparrow\downarrow} \neq 0$. This gives us a contradiction and we cannot find $\tilde{X}$ that would be universal across all systems. For each given $\hat{H}$, it will be possible to find $\tilde{X}$ from Eq. 32, but the result will not be the same for different systems. Another approach would be to search for the Einstein relation as a product of two or more different operators. This approach however leads to complicated derivative expressions and was not considered in this work.

Being only able to use the Green-Kubo definition of conductivity causes some limitations on the systems we can study. On top of the error in the time-evolution of the states, the size of the time steps also affects the accuracy of the integral giving us an additional source of error. The lack of Einstein relation also means that the mean square displacement between two channels has to be calculated separately, because it is required in the calculation of conductance, where some length scale has to be defined to get finite results. The most convenient way of calculating the MSD is to numerically integrate the spin-channel-specific VAC, because it has been calculated to access the conductivity. Of course this again accumulates error if the used time step is too large and limits the time range available in the calculation.

## 3.4 Spin transportation

In the Landauer-Büttiker formalism it is possible to define both spin-conserving and spin-flipping conductance [39] because it is linked to transmittance. Comparing the two spin-transport calculation methods, it would seem obvious that setting the two spins in Eq. 23 to up and down would give us spin flipping conductivity. While this does give some results, they cannot be directly compared to the ones given by Landauer-Büttiker.

The most problematic part in defining the spin flipping conductivity this way is that it fails to capture some, if not most, of the effects causing spin to flip. For example, spin flipping caused by potential defects is not shown at all by this quantity. This is caused by the definition of the velocity operator, $\hat{V}_\sigma = \frac{i}{\hbar}\hat{\sigma}_2[H,X]\hat{\sigma}_1$. The problem becomes apparent when we write out the commutator:

$$[H,X] = \sum_{\langle m,n \rangle} (X_n - X_m) H_{mn} |m\rangle\langle n|. \tag{38}$$

If $\hat{\sigma}_1 \neq \hat{\sigma}_2$, only one of the two off-diagonal blocks in the operator between the filters comes out non-zero. However, in the case of potential defects, $X_n = X_m$ and the surviving values are zero even before we apply the spin filter operators. Clearly the potential defects cause spin to flip and this definition of spin flipping current cannot be complete.

The lack of spin flipping current can be seen as a drawback of the tight-binding model: the up and down sites are assumed to reside at the exact same locations and when flipping occurs between them, the location of the electron stays the same. When the location does not change, there can be neither velocity nor conductivity. However, there are also differences between the two formalities and their perspectives to the scattering events. The

Kubo-Greenwood method focuses on the time evolution of wave packets and describes more what happens at each time step. Landauer-Büttiker on the other hand describes the end result of the scattering event, discarding the details on how the flipping occurs.

## 3.5 Spin polarization

When scattering is studied in a spinless case, calculating the conductivity often gives sufficient information. This is because conductivity is coupled to the mobility of the electrons and there are no additional degrees of freedom. This is not necessarily the case when spin is considered. Depending on the system being studied, it is possible to have spin and charge decoupled [40] and both of them have to be checked to see how the defects behave. Calculating the spin-polarized conductivity is one way of doing this, but it takes into account both spin polarization and electron mobility. It can be hard to distinguish between these two just from the conductivity and a way to study the amount of spin is required.

The simplest way of studying the behaviour of spin in the system is to look at the expectation value of spin filter operators $\hat{\sigma}_{\uparrow\downarrow}$ given by trace over the state vectors at different times. This quantity gives us the total amount of specific spin at each time step. Another possibility would be to look at the polarization, given by the expectation value of Pauli z-matrix $s_z = \hat{\sigma}_\uparrow - \hat{\sigma}_\downarrow$. While both of these approaches describe the total spin behaviour quite well, they don't provide any information about what happens at different energies.

To gain information about the energy, the trace has to be limited to states with certain energy. This can be done with a calculation similar to what we did with the conductivity:

$$S(E,t) = \frac{\mathrm{Tr}\left\{\delta(E-\hat{H})s_z(t)\right\}}{\mathrm{Tr}\left\{\delta(E-\hat{H})\right\}}. \tag{39}$$

The delta function projects the states to certain energy while the division by the density of states ensures that the polarization stays normalized. Because both conductivity and polarization can be calculated as function of time and energy, they can now be directly compared to see if there is a connection between spin and charge scatterings.

Calculating the energy projection can be problematic sometimes because it takes a lot of computational effort to get the delta function accurate enough. Sometimes it is enough to discard the energy information and just look at the average behaviour of the quantities. The easiest way of doing this is to calculate the time evolution of the probability density of an initial state. If we know the expectation value of an operator for each of the basis states and the probability of being in these states, the expectation value of the operator is simple to calculate:

$$\langle\hat{O}(t)\rangle = \sum_i \rho_i(t)\langle\psi_i|\hat{O}|\psi_i\rangle. \tag{40}$$

It is straightforward to calculate the spin polarization when density is known because the expectation values $\langle\psi_i|\hat{s}_z|\psi_i\rangle$ are either 1 or -1, depending on whether the state $\psi_i$ is up or

down. Conductivity, on the other hand, is a bit trickier to calculate. In order to calculate it, we need information about either the velocity or displacement of the electrons. The problem is that we evolve the system as a whole and cannot track the density evolution for individual sites. While we know the change in density for each site, we do not know where it came from or goes to.

This problem can be resolved by using a localized initial state. We still don't know the exact details of the density evolution, but since the initial location is known, the displacement from the initial location of the packet can be calculated. The displacement for each site can be squared and inserted into Eq. 40 to get the MSD for the system. One slight problem in this approach is the finite size of the simulation area. The velocity of ballistic electrons in graphene is so high that the boundaries are reached relatively fast, after which the wave packet is transferred to the opposing side due to the periodic boundary conditions. Therefore the best results are gained by placing the initial state to the center of the system and only considering the results from the time before the wave packet hits the boundaries for the first time. This way we don't have to worry about the fact that the displacement is bounded by the size of the system.

# 4 Implementation

## 4.1 Numerical approximations

The implementation is mostly based on the process described in [29]. There are three main approximations that are required to achieve linear scaling algorithm. The first one is to replace the trace with a sum over random vectors and the two others are to approximate the delta function and the time evolutions with a Chebyshev expansion.

The trace operation is defined as the sum of the diagonal elements of an operator. This requires computational effort scaling as $O(N^2)$, because the inner product $\langle\psi|\hat{O}|\psi\rangle$ has to be calculated for each vector in the basis. To reduce the scaling to $O(N)$, the trace is replaced with a sum over random vectors:

$$\mathrm{Tr}\{\hat{O}\} \approx \frac{1}{N_r}\sum_{i=0}^{N_r-1}\langle\psi_i|\hat{O}|\psi_i\rangle, \tag{41}$$

where the vectors $|\psi_i\rangle$ are random-phase states, defined as $\langle j|\psi_i\rangle = e^{i\phi_{ij}}$ with $\phi_{ij}$ being random, independent numbers. These states sample the full spectrum and it can be shown that the expectation value of these inner products gives the trace [41]. It can be shown that the error of the estimate is $O(1/\sqrt{N_r N})$, which means that even a small number of random vectors $N_r$ can give a good estimate as long as $N$ is large enough.

There is no analytical formula for the delta function, which means it has to be approximated numerically. There are multiple different methods of doing the approximation, such as the

Lanczos recursion method (LRM), the Fourier transform method (FTM) and the kernel polynomial method (KPM). The method of choice for this work is the KPM.

The kernel polynomial methods include a wide range of techniques involving expansion of a function in polynomial bases. In practical implementations these expansions have to be limited to finite amount of basis functions, which causes bad behaviour, known as Gibbs oscillation, to occur if the function being expanded is not nice enough. The solution is to introduce a kernel function to the expansion, suppressing the oscillation.

The basis of choice in our work is the set of Chebyshev polynomials, which means a function can be written as

$$f(x) = \frac{1}{\pi\sqrt{1-x^2}} \sum_{-\infty}^{\infty} \mu_n T_n(x), \tag{42}$$

where $\mu_n = \int_{-1}^{1} f(x) T_n(x)$ and the Chebyshev polynomials $T_n$ are defined recursively as

$$T_n(x) = 2xT_{n-1}(x) - T_n(x) \tag{43}$$

$$T_{-n} = T_n, \tag{44}$$

starting from $T_0(x) = 1$ and $T_1(x) = x$. In our case the function we want to approximate is a delta function, giving us $\mu_n = T_n(\hat{H})$. If we now insert Eq. 42 into 23, the velocity autocorrelation function becomes

$$\rho(E) C_{vv}(E,t) = \frac{1}{\pi\Omega\sqrt{1-E^2}} \sum_{n=0}^{\infty} (2 - \delta_{n0}) T_n(E) C_n^{VAC}(t), \tag{45}$$

where $C_n^{VAC}(t)$ are the Chebyshev moments for velocity autocorrelation:

$$C_n^{VAC}(t) \approx \sum_i \mathrm{Re}\left\{ \langle \psi_i | \hat{V}_{\hat{\sigma}}(t)^\dagger \hat{V}_{\hat{\sigma}} T_n(\hat{H}) | \psi_i \rangle \right\}. \tag{46}$$

Other quantities, such as the density of states and the mean square displacement, can also be written in a similar fashion by replacing the velocity autocorrelation function with a corresponding expression in the Chebyshev moments.

The Gibbs oscillations arise in the truncation of the expansion when the function being expanded is not continuously differentiable. Delta function is certainly not smooth enough to fit in this criterion, which means that something has to be done to counter the oscillations. One way of doing this is to apply damping coefficients $g_n$ to the sum:

$$\rho(E) C_{vv}(E,t) \approx \frac{1}{\pi\Omega\sqrt{1-E^2}} \sum_{n=0}^{N_m} g_n (2 - \delta_{n0}) T_n(E) C_n^{VAC}(t). \tag{47}$$

In this work the Jackson kernel is used, for which

$$g_n = (1 - n\alpha)\cos(\pi n\alpha) + \alpha \sin(\pi n\alpha)\cot(\pi\alpha), \tag{48}$$

with $\alpha = 1/(N_m + 1)$.

The third approximation is considering the time evolution. The time evolution operator is a matrix exponential and thus cannot be applied exactly, except for special cases. To find a numerical approximation for the evolution, we again use the Chebyshev polynomials to expand the operator, which becomes

$$\hat{U}(\Delta t) \approx \sum_{m=0}^{N_p-1} (2 - \delta_{n0})(\mp i)^m J_m \left( \frac{\Delta t}{\hbar} \right) T_m(\hat{H}), \tag{49}$$

where $J_m$ are the Bessel functions of the first kind. A similar formula can also be found for the commutator of the position operator and the time evolution operator, required in the calculation of mean square displacement:

$$[\hat{X},\hat{U}(\Delta t)] \approx \sum_{m=0}^{N_p-1} (2 - \delta_{n0})(\mp i)^m J_m \left( \frac{\Delta t}{\hbar} \right) [\hat{X}, T_m(\hat{H})], \tag{50}$$

At first glance the expansions look slightly different compared to the expansion used with the delta function. This is however only a matter of definition of the basis: the sets $\{T_n(x)\}$ and $\left\{ \frac{T_n(x)}{\pi\sqrt{1-x^2}} \right\}$ both form orthonormal basis and the difference in the expansions is only a matter of choice between these two.

Even though Eq. 46 is perfectly valid equation for the calculation of Chebyshev moments, it's not a practical one. The time evolution is included in one of the velocity operators and cannot be applied efficiently. To make the situation better, cyclic properties of trace can be used to write the equation in a more suitable form:

$$C_n^{VAC}(t) \approx \sum_i \mathrm{Re} \left\{ \langle \psi_i | \hat{U}(t) \hat{V}_{\hat{\sigma}} T_n(\hat{H}) \hat{U}^\dagger(t) \hat{V}_{\hat{\sigma}}^\dagger | \psi_i \rangle \right\}. \tag{51}$$

Writing the time evolution operators explicitly makes it possible to apply them directly to the vectors, saving both computation time and memory. To further reduce the time required for the calculation of time evolution, we use the property $U(t+\Delta t) = U(t)U(\Delta t)$. This allows us to use recursive formulas in the calculation:

$$\langle \psi_i | \hat{U}(t + \Delta t) \hat{V}_{\hat{\sigma}} = \langle \psi_i | \hat{U}(t) \hat{U}(\Delta t) \hat{V}_{\hat{\sigma}} \tag{52}$$

$$\hat{U}^\dagger(t + \Delta t) \hat{V}_{\hat{\sigma}}^\dagger | \psi_i \rangle = \hat{U}^\dagger(\Delta t) \hat{U}^\dagger(t) \hat{V}_{\hat{\sigma}}^\dagger | \psi_i \rangle. \tag{53}$$

Keeping $\langle \psi_i | \hat{U}(t)$ and $\hat{U}^\dagger(t) \hat{V}_{\hat{\sigma}}^\dagger | \psi_i \rangle$ in memory after each time step makes computation of the next step much easier because we can use the previous result to compute the next one.

Because of the similar form of the quantities being calculated, it is straightforward to generalize the calculation of VAC to the others. The only difference between them is in the Chebyshev moments and even they look quite similar. The easiest quantity to calculate is the density of states because it doesn't depend on time:

$$C_n^{DOS} \approx \sum_i \langle \psi_i | T_n(\hat{H}) | \psi_i \rangle. \tag{54}$$

The lack of time dependence comes from the fact that $\hat{U}$ is unitary and it also commutes with the delta function. The calculation of spin polarization is almost as easy. The only difference is that we have $s_z$ included and it does not commute with the time evolution operator:

$$C_n^S(E,t) \approx \sum_i \langle \psi_i(t)|T_n(\hat{H})s_z|\psi_i(t)\rangle. \tag{55}$$

For the MSD, the process is a bit more complicated as the time evolution cannot be moved next to the state vectors. We would like to end up with a symmetrical form and the best way to do so is to cycle the time evolution so that we end up with its commutator with the operator $\hat{X}$:

$$C_n^{MSD} \approx \sum_i \langle \psi_i|[\hat{X},\hat{U}(t)]^\dagger T_n(\hat{H})[\hat{X},\hat{U}(t)]|\psi_i\rangle. \tag{56}$$

Because the expressions on either side of the Chebyshev polynomial are conjugates of each other, it is enough to calculate one of them. The calculation is made easier by using the properties of time evolution and re-writing the commutator:

$$[\hat{X},\hat{U}(t+\Delta t)]|\psi_i\rangle = \hat{U}(\Delta t)[\hat{X},\hat{U}(t)]|\psi_i\rangle + [\hat{X},\hat{U}(\Delta t)]\hat{U}(t)|\psi_i\rangle. \tag{57}$$

This equation allows recursive calculation of the MSD, with the help of Eq. 50.

## 4.2 GPU acceleration

The most computationally intensive part of the Chebyshev expansion is the moment calculation, as it involves applying the Hamiltonian multiple times to states. The reason for good performance of the GPUs lies in the relatively high arithmetic intensity of matrix-vector multiplication. Most of the algorithms used can be implemented on the GPU, minimizing the amount of memory transfer to and from the GPU memory. In fact, the memory transfers are only required during the initialization phase and when we return the calculated Chebyshev moments back to the CPU memory.

During the initialization phase, the Hamiltonian and the initial random state vector are transferred to the GPU. The Hamiltonian stays constant for the whole duration of the calculation and it is enough to transfer it only once. The random states are generated on the CPU and as the calculation loops through multiple random states, we transfer the current one at the beginning of each loop. It might be slightly more efficient to generate them on the GPU, but since it takes only a fraction of the total computational time, the generation may as well be done on the CPU. Generating the initial state on the CPU is slightly more flexible and allows different initial states be generated more easily.

The most crucial part of the calculation is to implement the operations $|\psi_{out}\rangle = \hat{H}|\psi_{in}\rangle$ and $\psi_{out}\rangle = [\hat{H},\hat{X}]|\psi_{in}\rangle$ as efficiently as possible, as the most time is spent on them in the Chebyshev moment calculation. The elements of $|\psi_{out}\rangle$ are independent of each other during the matrix-vector product and it is natural to parallellize the calculation over the elements of the output vector. With GPU this is easily done by launching threads equal

to number of elements and letting each thread calculate one element of the result. As the number of threads is massive, the order in which they access memory will affect the performance greatly. This mostly concerns the sparse Hamiltonian and there are two ways of ordering its data in memory. For CPUs using sequential code, the better way would be that all data for single site are next to each other and these blocks of data would be ordered by the index of the sites. However, for GPUs it's better to group the data by their neighbour index, such that all 0th neighbours come first in the site index order, followed by 1st neighbours and so on. This way consecutive threads access consecutive data in the memory, leading to more efficient use of memory [42].

The performance of the original GPU implementation has been studied to more extent in [29]. The overall speedup factor compared to a serial CPU implementation was reported to be around 16. Even though this is much smaller than speedup for some other cases [43], it is still remarkable. Reaching this speed on CPUs would require a lot of effort because in the ideal case, the number of required processor cores would be 16. Typically the frequency of a processor decreases with increasing number of cores [44], causing even higher number of cores to be required to reach the same speed.

# 5 Results

To test the methods described above, graphene was chosen as the platform to contain the defects in. It has little effect on spin and its properties are well described by simple tight-binding model, making it ideal material to test our implementation with.

Two different samples were used in the testing. A $1000 \times 1000$ cell with periodic boundary conditions was used to model pristine graphene. The number of atoms was chosen large enough to model an ideal graphene lattice, while keeping the computation time moderate. Some tests were also run on a $65000 \times 16$ sample, simulating a zigzag nanoribbon. In the latter case the periodic boundary conditions were applied only in the longer of the two dimensions.

## 5.1 Pristine Nanoribbons

If there are no spin scattering defects in the system, there should be no differences between the results of spinful and spinless calculations. To confirm this in our implementation, the conductance of pure graphene nanoribbon was calculated. The conductance in graphene nanoribbons is quantized and it should get values that are multiples of the conductance quantum $\frac{e^2}{h}$ [45].

The Landauer-Büttiker formalism is able to recover the quantization easily, but Kubo-Greenwood, which we are using, requires some additional effort. Transport in pure graphene is ballistic, which causes conductivity to diverge. To get a finite value for conductance, a

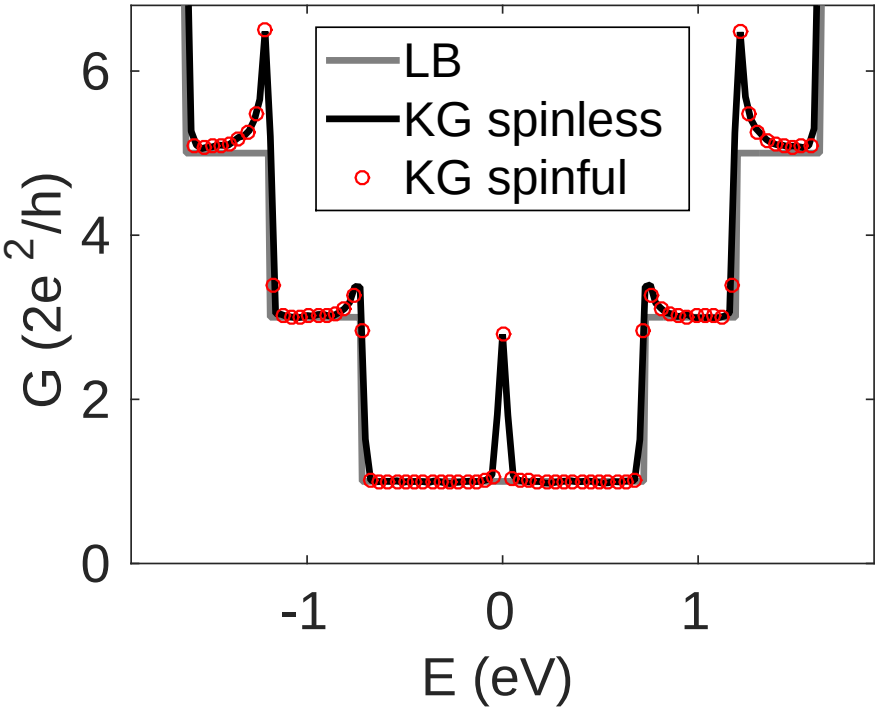


Figure 2: Total conductance of 65000×16 graphene nanoribbon calculated using Landauer-Büttiker formalism and both spinless and spinful versions of Kubo-Greenwood.

length scale has to be introduced. A common way of doing this is to define conductance as

$$G(E) = \frac{W}{L(E,t)}\sigma(E,t), \tag{58}$$

where $W$ is the width of the system and $L(E,t)$ is length calculated from MSD:

$$L(E,t) = 2\sqrt{\Delta X^2(E,t)}. \tag{59}$$

Both $L$ and $\sigma$ are expected to grow linearly in time during ballistic transport, which means $G$ should converge to a finite value.

The calculated conductance of the 65000×16 nanoribbon can be found in Figure 2. In addition to the implementation being tested, the conductance has also been calculated using two methods. The first one of them is a spinless implementation of Kubo-Greenwood formalism, the code upon which our spinful Kubo-Greenwood has been built on. The second one uses non-equilibrium Green's functions (NEGF) and is based on the Landauer-formalism. The NEGF gives the smoothest result of the three because it doesn't use stochastic methods and can be regarded as an exact method within the tight-binding approximation.

All three methods show the quantized conductance levels. The actual step-like behaviour is nicely recovered by the NEGF, for which the conductance is precisely an integer times the

conductance quantum. Both Kubo-Greenwood methods overshoot the conductance near the band edges, but they stabilize to the value give by NEGF further away from the edges. This behaviour is expected and it is caused by the singular behaviour of both DOS and electron velocity near the band edges. The spinful calculation agrees quite well with the spinless one and the differences are mostly explained by the difference in the energy points used in the calculation.

## 5.2 Spin-Dependent Potential in Nanoribbons

In our previous work [19] we studied nanoribbons with defects which had spin-dependent potential on a single atom site. These systems have almost ballistic transport, having only a small range of energy for each spin that causes scattering. The scattering is strongest when the defect is located on the edge of the ribbon and gets weaker as the defect is moved towards the center. An example of conductivity for this kind of ribbon can be seen in Figures 3a and 3b, where a single defect has been placed on the edge and in the middle of the ribbon. The potential has been chosen to be $\pm 2$ eV and the defect angle $\theta$ is set to 0, giving no coupling between the spins.

The Kubo-Greenwood method would have trouble with the system used in calculating these Figures, because they have only one defect in them. The method is more suitable for systems with uniform defect placement as the random vectors sampling the system are more likely to hit the defects. Because of this, the number of random vectors required for a single defect site is too large and the computational effort required is too much. Instead, a system with 0.01% defect concentration was used to compare the spin-dependent conductivity. The potential strength was still kept at $\pm 2$ eV and the angle $\theta$ at 0, but the defect placement was not restricted to the edges. The results are shown in Figures 3c.

Even though the results differ from each other, the main features are common for both of the methods. The quantization of conductance is still present, even though the defects are causing the steps to smoothen out a bit. The placement of the defect has major impact on the results. When the defect is on the edge, the most interesting parts in the energy spectrum are at $\pm 0.4$ eV, where one of the spin channels has a dip in conductance, while the other stays constant. In the middle of the ribbon, the defect has almost no effect on the conductance. For the Kubo-Greenwood calculation, the dips appear at the exact same energies for both methods even though they are barely visible. The differences between the methods can be explained by the different systems from which the results were obtained. The randomization of the defect placement causes the result to be average of the bulk and edge cases and the depth of the dips is decreased.

The same calculations were also done for a higher defect concentration of 1%. This also gave similar behaviour, where the conductance has a dip near $\pm 0.4$ eV. However, the problem with this system is that the transport becomes diffusive and Equations 58 and 59 cannot be used reliably any more. Instead of saturating to certain level, the conductance keeps on decreasing. No further analysis was done for the higher concentration once the diffusivity

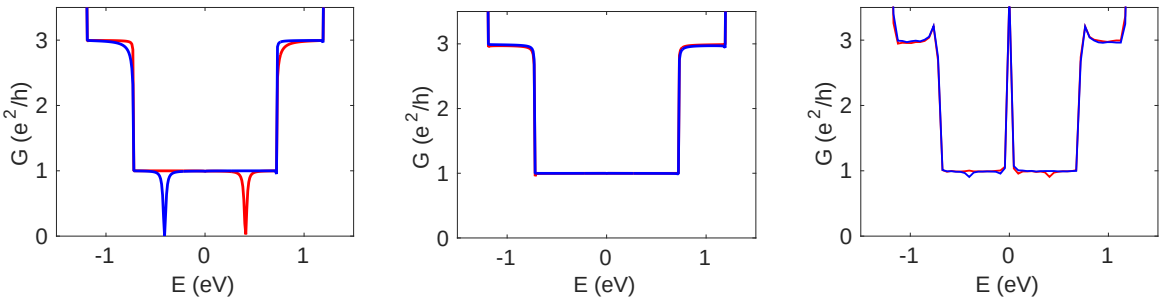


(a) Landauer-Büttiker, edge (b) Landauer-Büttiker, bulk (c) Kubo-Greenwood

Figure 3: Conductance of nanoribbon with defects having a spin-dependent potential.

was discovered, but the location of the dips supports the results gained from the lower concentration.

The situation changes slightly when the angle of the defects is changed to 90°. The potential is now a local coupling between the spin channels and both channels now behave identically. The coupling allows spin to flip and it is now meaningful to calculate the spin polarization as a function of time, in addition to the conductance. The defect phase $\phi$ is kept constant at 0° to keep the calculations simple.

A conductance comparison between the two methods can be seen in Figure 4a. To make the comparison better, there are now two defects in the Landauer-Büttiker calculation and the result has been averaged over multiple configurations. Also, the Landauer-Büttiker makes it easy to define spin-flipping transmittance, which is also shown in the figure. For Kubo-Greenwood, only the spin conserving conductance was calculated and the shown data is taken as an average between the conductances of the two spins. The results converge slowly and taking the average allows to get a better result a bit faster.

The conserving conductances agree quite well with each other. There is still some noise in the Kubo-Greenwood calculation, but the biggest dips are located at the same energies as they are in the Landauer-Büttiker. Both methods also recover the quantization quite well, even though the defects are already causing the levels to deviate from the original step-like structure.

Since Kubo-Greenwood cannot calculate spin flipping conductance the same way Landauer-Büttiker can, spin polarization was calculated instead. Figure 4b shows the amount of spin polarization after 5 ps, starting from completely down-polarized initial state, for which $S(E,0) = -1$. An exponential function was fitted to the first 0.5 ps of the simulation for each energy and the inverse of the fitted time constant is also shown in the figure. The flipping conductance calculated by the Landauer-Büttiker method is shown as a comparison in the same figure.

Between these three sets of data, there is most correlation between the inverse of the time constant and the flipping conductance. Both of these two are peaked at the same energies

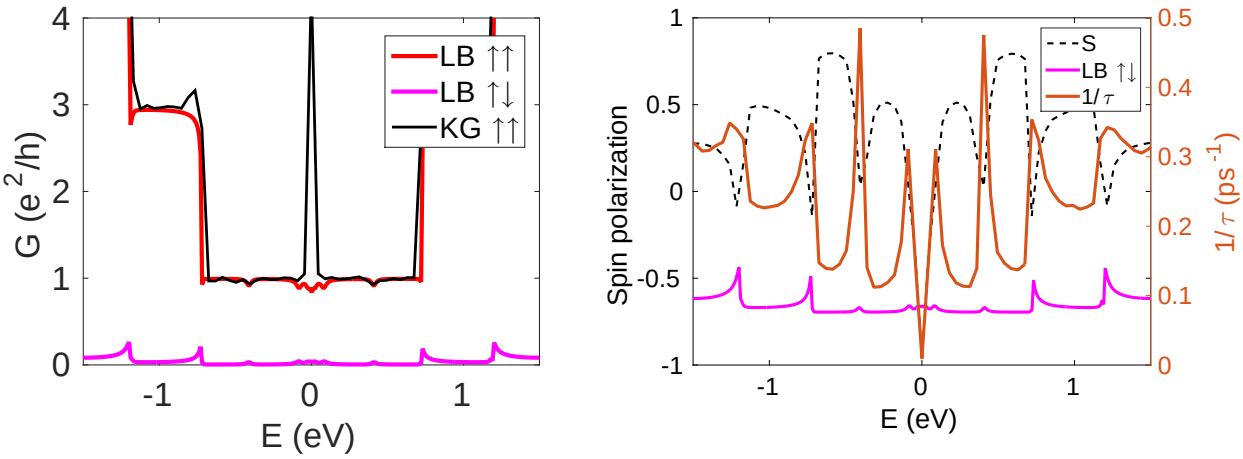


(a) Conductance

(b) Spin polarization and time constant

Figure 4: Conductance, spin relaxation time, and spin polarization for potential defects in nanoribbons. Figure (a) shows a comparison between different conductances, while (b) shows the spin polarization at $t = 5$ ps and the time constant fitted for the first 0.5 ps of the simulation. The flipping conductance in (b) is the same data as in (a), slightly scaled to give better comparison.

and behave roughly the same way between the peaks, the only exception being the energies near zero. The spin polarization on the other hand seems to behave exactly the opposite way as it has minima at the same energies where the other two are peaked.

The seemingly different results stem from the considerably different behaviour of spin polarization for different energies. At the resonant energies of the defects, the band edges and $\pm 0.4$ eV, the polarization goes directly to zero and the flipping rate is fast right from the start. As the polarization gets closer to zero, the rate slows down and there is barely any oscillation. The non-resonant energies initially flip the spin much slower, as seen from the inverse of the time constant. The rate however increases with time and polarization starts to oscillate around zero.

The energy range from -0.1 eV to 0.1 eV replicates the Landauer-Büttiker results the worst, as there is barely any spin flipping at $E = 0$, even though there should be some. The peaks at $\pm 0.09$ eV roughly correspond to the peaks in conductance, but between them the time constant gets larger than it should. Its inverse behaves almost identically to the spin polarization, unlike in any other energy. This anomaly is most likely caused by the band structure near the Dirac point. Because the sample is a zigzag ribbon, there are localized edge states at $E = 0$. The localization causes the quantities to go to zero, as the electrons with these energies can not sample the system as well.

The edges have a big impact on the nanoribbons' results. Landauer-Büttiker shows largest dips in the conductance when the defects are placed on the edge and the edge states near zero energy have been hard to reach using Kubo-Greenwood. To further analyse the edges,

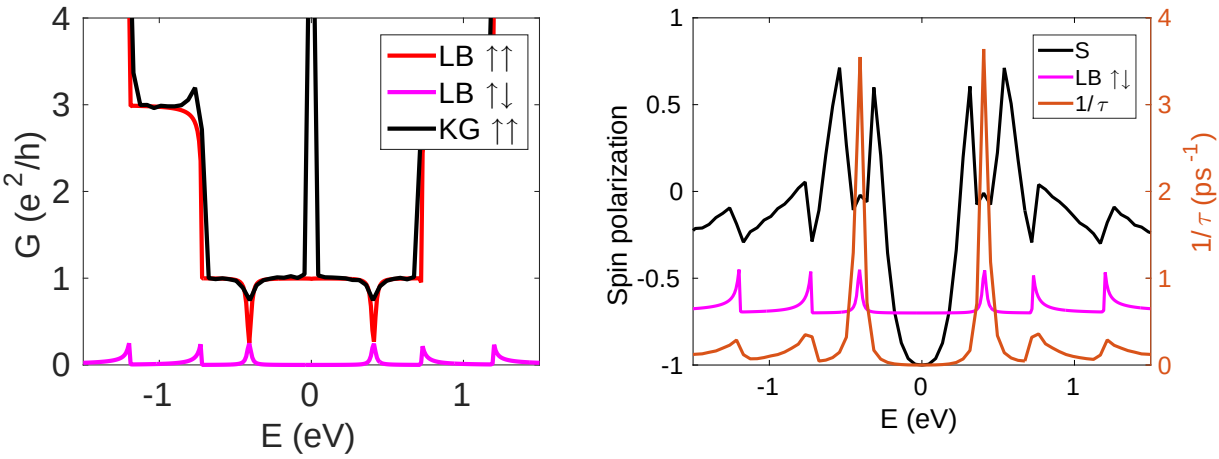


(a) Conductance

(b) Spin polarization and time constant

Figure 5: Conductance, spin polarization and inverse time constant for ribbon with defects placed on the edge.

the spin polarization and conductance were calculated such that the defects were only placed on the edges of the system. The results are shown in Figure 5.

The change in the results is remarkable. The difference in conductance between Landauer-Büttiker and Kubo-Greenwood is now much smaller, as the dips are clearly visible also in the Kubo calculation. Their magnitude is still not as large as in the Landauer calculation, but compared to the previous case, they are now much more visible. The different defect placement also affected the Landauer-Büttiker results a bit. There is no longer anything happening near $E = 0$ and only the energies $\pm 0.4$ eV and the band edges show deviation from the step structure.

Even more radical changes can be seen in the spin polarization. The resonant energies at $\pm 0.4$ eV had already higher flipping rate than other energies, but this time the inverse of the time constant is roughly 10 times larger than in the previous case. The polarization at these energies still behaves the same way, going directly back to zero and showing no oscillation. In the higher energies the relaxation time doesn't change much and the differences are mostly seen in the amount of spin polarization. This time most of the energy range doesn't have any oscillation for the polarization, except for the energies around resonance. The most curious change however is the behaviour near zero. Instead of the linear, rather sharp drop to zero, $1/\tau$ and spin polarization tend to zero in a much smoother way. Again, the changes are most likely caused by the edge states. The potential added to the edge sites disrupts the state and difference in the behaviour can be expected.

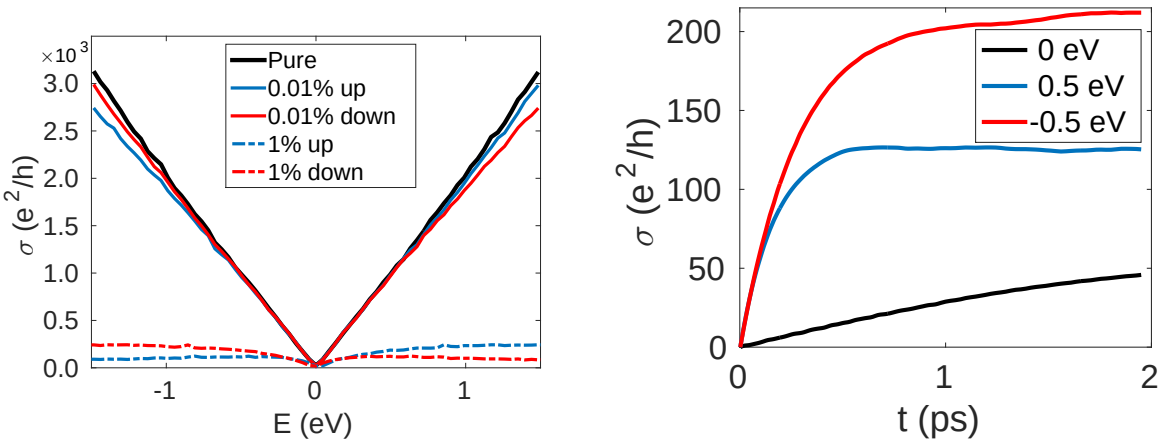


(a) (b)

Figure 6: (a) Conductivity for pure graphene and potential defects at concentrations of 0.01% and 1%. Conductances for pure graphene and low concentration have been measured at propagation length of 1000 nm, while the higher concentration is taken from $t = 0.6$ ps. (b) Conductivity as a function of time at different energies for 1% concentration.

## 5.3 Spin-Dependent Potential in Graphene

### 5.3.1 Spin conserving potential

Even though Kubo-Greenwood method produces correct results in the nanoribbons, it is outperformed by the Landauer-Büttiker method. The geometry of the system causes the results to converge slowly, because the long but narrow shape limits the amount of system each random vector can sample. Another thing to consider in the ribbons is the presence of the edge states. Because the zigzag edge states are localized, the Kubo-Greenwood method has trouble reaching them.

All of these problems can be avoided by moving to a 2-dimensional system. In regular graphene we don't have to worry about the limitations given by the narrow system and the lack of edge states makes the calculation easier. This wide systems cannot be reached by the Landauer-Büttiker method, as it scales cubically with respect to the width of the system, and Kubo-Greenwood becomes better of the two methods. Taking graphene as a platform for defects makes it easier to look into intrinsic properties of the defects. With periodic boundary conditions, there is virtually no contribution from edges and the large system size further reduces the finite-size effects.

We start with the same potential defects we used with the ribbons. To keep the results comparable to the previous ones, the strength of the spin-dependent potential is kept the same, at $\pm 2$ eV. We also start with the same defect concentration of 0.01%, but this time we also look into higher concentrations in more detail.

As seen in Figure 6a, the potential defects do not affect the conductance much in low concentrations. The conductance is slightly smaller with defects in the system, but the overall behaviour stays the same in the shown energy range. The difference becomes larger at higher energies, but since they are already outside of the valid range for tight-binding approximation, they are not analysed further. As the concentration goes up, the difference becomes apparent. While the transport is ballistic in the lower concentration, this is no longer the case in the higher concentration. The conductivity does not diverge, but saturates to some levels, depending on the energy. Because of the saturation, there is no need to measure the conductivity at constant length scale. In fact, the length at which the other conductivities were measured, 1000 nm, was not reached in the whole energy range by the end of the simulation time, 2 ps. The longer simulation time required to reach this length would make the simulation run considerably longer since shorter time steps would have to be used to minimize the error made in the time evolution.

The main observation from the behaviour of the potential defects is that the conductivity becomes asymmetric with respect to the zero energy. The two spin-channels are symmetric to each other, but inside each of them the symmetry is broken. The conductivity becomes smaller on the side at which the potential is, for example in Figure 6a the up-conductivity is smaller at negative energies when the potential strength for up-sites is -2 eV. The relative difference is modest in the smaller concentration, but it becomes considerable in the larger concentration.

Figure 6b shows the time evolution of conductivity at $E = 0$ eV and $E = \pm 0.5$ eV for the higher concentration of defects. For $E = \pm 0.5$ eV the saturation is already seen, but at zero energy, the maximum is not yet reached. Longer simulation would be needed to see whether the conductance stays on the saturated level or starts decaying. Because of poor convergence, the simulation time had to be limited to a maximum of 2 ps, as convergence required more random vectors than usually. The problems with convergence are caused by the fluctuations of the conductivity, which is seen in the diversity of the results calculated using single random vectors. Some vectors behave almost ballistically, while others show behaviour with decaying conductance. When the average is taken over multiple random vectors, the result becomes diffusive and saturation is observed.

One way of improving the convergence would be to use lesser amount of Chebyshev moments in the calculation. The results in Figure 6 were calculated with $N_m = 3000$, a considerably high value. Higher number of moments ensures all features are captured in the results, but it also makes noise more significant. Lowering the amount would smoothen the results with respect to energy and most of the energy range would see improvement in the results. The problematic part is the energies near zero. As seen in Figure 6a, there is a kink in conductivity at the zero energy where the linear slopes meet each other. If the number of moments was decreased, the conductivity would behave smoothly also at zero. This is unwanted behaviour as the conductivity near zero would gain way too large value. The effect of the number of moments is studied more later.

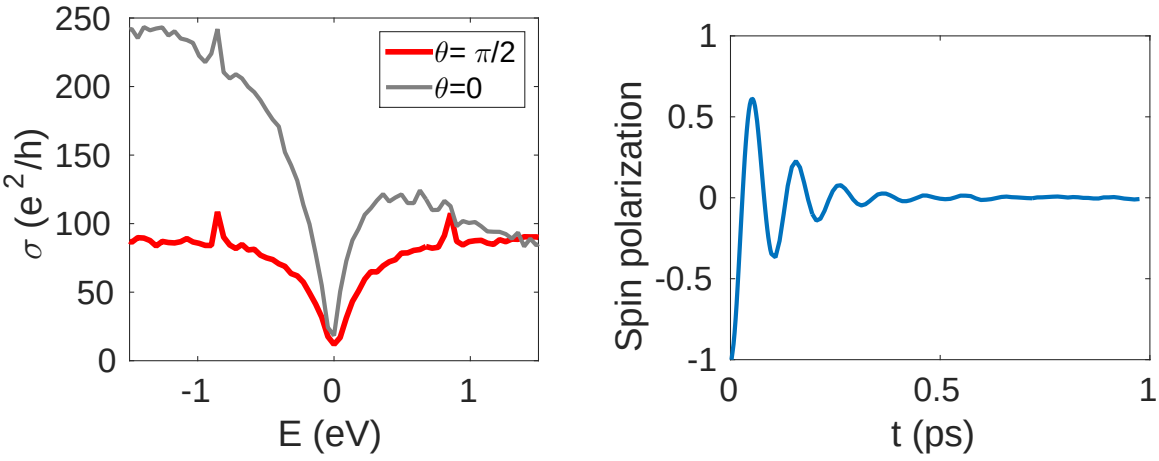


(a) (b)

Figure 7: (a) Down-spin conductivity for potential defects in graphene with two different defect angles, both measured at $t = 0.6$ ps. (b) Spin polarization as a function of time at $E = 0.5$ eV. Both figures are for graphene with 1% concentration of potential defects.

### 5.3.2 Spin flipping potential

The conductance behaves a bit surprisingly when the defect angles are turned to $\pi/2$. Both up and down conductivities have the same value as expected, but as seen in Figure 7a, the value is smaller than either of the conductivities in the $\theta = 0$ case. This is considerably different behaviour than for the lower concentration of defects in nanoribbons, for which the conserving conductance at $\theta = \pi/2$ was much more like average of the up and down conductances from $\theta = 0$. The results of the figure are calculated for 1% concentration, which may explain the difference as the ribbons results were taken from 0.01%. Differences in the charge carrier mobility do not affect the results, because the results are the same regardless of whether the conductivity is measured at constant time or length. In any case, the coupling between up and down sites seems to be causing more charge scattering than the corresponding spin-conserving potential, leading to smaller conductance.

When the spin polarization for 1% concentration is calculated, it is now apparent that it behaves as a damped oscillator, described by equation

$$S(t) = -e^{-t/\tau}\cos(\omega t), \tag{60}$$

where $\tau$ is the time constant for damping and $\omega$ is the angular frequency of the oscillation. As seen in Figure 7b, the polarization goes to zero quite fast, but a clear sinusoidal oscillation is observed before that happens. This questions the exponential fit made to the polarization in ribbons earlier. It is possible that the behaviour in the ribbons also follows Eq. 60 instead of simple exponential decay, but since the fit was then made only for the beginning of the simulation with no present oscillation, the results should still be valid.

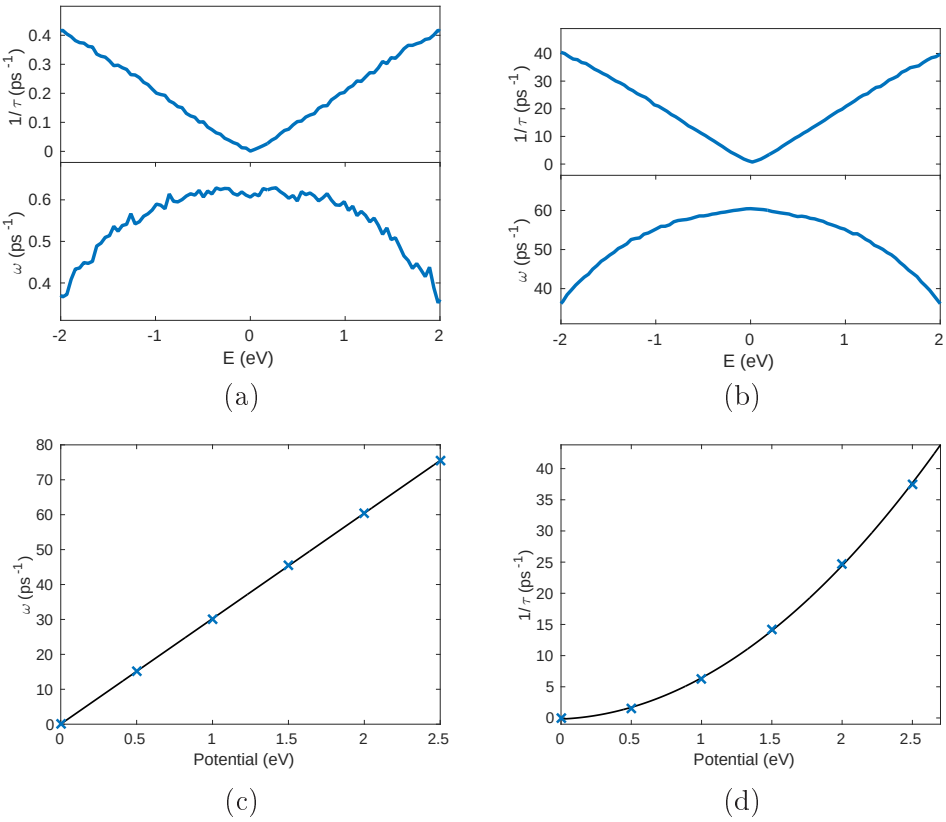


Figure 8: (a, b)Fitting parameters $\omega$ (lower) and $\tau$ (upper) from Eq. 60 for potential defects with $\theta = \pi/2$ and potential strength $\pm 2$ eV in graphene. The defects concentrations are 0.01% and 1%. (c) Spin precession speed $\omega$ measured at $E = 0$ eV for different potential strengths. (d) Inverse of spin relaxation time $\tau$ measured at $E = 1$ eV. The solid black lines in last two figures show linear and quadratic fits to the data points.

Figure 8 shows the fitting parameters as a function of energy for both 0.01% and 1% concentrations of potential defects in graphene. Unlike with the ribbons, there are no resonant energies for the defects where the behaviour would be special in some way. This supports the observation that the resonant energies for ribbons were caused by the edge states of the system. Edges have a much smaller role in the graphene and periodic boundary conditions make them even less important, fading away the possible small contributions of edge states.

When the results of the two concentrations are compared, their similarity is astounding. The time constants have completely different magnitudes in the two systems, but their behaviour is exactly the same. The smaller concentration does have slightly more roughness in the shape, but this is most likely caused by the slower oscillation in the system. When there is barely any oscillation during the time for which the fit is made, it is harder to do the fit accurately.

Another curious observation is that the ratio between the results at each energy is remarkably close to 0.01, the ratio of the defect concentrations. This suggests that both of the (inverse) time constants scale linearly with respect to the defect density. This behaviour is also encountered with other similar spin-flipping systems [46].

So far all of the potential defects calculations have been made with the same potential strength, $\pm 2$ eV. While this has given pretty good results, the effect of different potential strengths should also be checked. To do this, the calculations were repeated while the strength was varied from 0.5 eV to 2.5 eV. Spin polarization still shows damped oscillatory behaviour throughout the whole range and both time constants behave the same as a function of energy. The values of the constants at selected energies can be seen in figures 8c and 8d. For $\omega$ the values are taken from $E = 0$ eV and for $\tau$ they are from $E = 1$ eV.

The time constants seem to obey simple linear and quadratic scaling, as seen from the fits done to the data. The linear scaling of $\omega$ is expected, as oscillation speed usually depends on the energy difference between the two states between which the oscillation is happening [47]. Since we are controlling the potential for each spin channel, we are essentially changing their energies, leading to the linear scaling. The quadratic behaviour of $\tau$ on the other hand can be explained by the mechanisms causing spin scattering. The two conventional mechanisms are called Elliot-Yafet (EY) and Dyakonov-Perel (DP) [48]. Both of them scale the spin relaxation time as $\tau_s \sim 1/\Delta^2$ with $\Delta$ being the potential difference between spin channels [49, 50], explaining the observation. The dominant mechanism of the two is usually discriminated by the relative behaviour of $\tau$ and $\tau_p$, the momentum relaxation time [51]. In our case, we cannot use this information to specify the underlying mechanism because the two relaxation times are uncoupled. Nevertheless, the fact that both mechanisms have a similar scaling with respect to potential strength supports our results.

## 5.4 Adatom Plaquettes

The potential defects studied in the previous section should be considered purely as mathematical defects. While something similar could be achieved with e.g. light adatoms on top of the carbon atoms, the potential strength is quite strong for any viable real-world defects. Additionally, real world defects will most likely affect multiple sites and can be more complicated than simple spin-dependent potential on single sites.

One way to approach the more realistic spin relaxation methods is the so-called Rashba field, which can be seen in the tight-binding Hamiltonian as complex spin-flipping hoppings. The Rashba Hamiltonian is given by

$$\hat{H}_R = iV_R \sum_{\langle i,j \rangle} \vec{z} \cdot (\vec{s} \times \vec{d}_{ij}) |i\rangle\langle j|, \tag{61}$$

where the sum goes over the nearest neighbours affected by the Rashba field, $\vec{z}$ is unit vector normal to the plane, $\vec{s}$ is vector formed from Pauli matrices and $\vec{d}_{ij}$ is unit vector along the bond between sites $i$ and $j$. The Hamiltonian may seem a bit complicated, but

when written out in the spin basis, the terms being summed have actually quite simple form

$$\begin{bmatrix} 0 & -\cos\phi + i\sin\phi \\ \cos\phi + i\sin\phi & 0 \end{bmatrix}, \tag{62}$$

where $\phi$ is the angle between the bond and the x-axis. It is easy to see from this form that the spin-flipping hoppings have constant magnitude, but their complex phase depends on the orientation of the bond.

It has been observed experimentally that Rashba field can be induced by heavy adatoms, such as gold, sitting in the hollow sites of graphene lattice [52]. This type of Rashba effect has been studied by van Tuan *et al.* [46]. In the model they used, a gold adatom sitting in the middle of graphene hexagon induces a Rashba field to the surrounding carbon sites. In addition to the Rashba part, they also include intrinsic spin-orbit coupling and a potential shift associated with the adatoms. The Hamiltonian used has the form

$$\hat{H} = H_0 + \frac{2i}{\sqrt{3}} V_I \sum_{\langle\langle i,j\rangle\rangle \in \mathcal{R}} \vec{s} \cdot (\vec{d}_{kj} \times \vec{d}_{ik}) |i\rangle\langle j| + H_R - \mu \sum_{i \in \mathcal{R}} |i\rangle\langle i|, \tag{63}$$

with $\mathcal{R}$ being the set of plaquettes next to the adatoms and $\langle\langle i,j\rangle\rangle \in \mathcal{R}$ denoting the next-nearest hoppings within the plaquette. The intrinsic spin-orbit coupling can be written out similar to what was done with the Rashba part and it simply induces a spin-dependent 2nd-nearest neighbour hopping within the plaquette. The hoppings become $\pm i/\sqrt{3} V_I$ and there is no coupling between the opposing spins. The local potential shift is needed because there is a local charge redistribution due to the adatoms [53].

Our results for the spin behaviour agree qualitatively with the ones van Tuan *et al.* had in their paper, as seen in Figure 9a. The spin relaxation time features an M-shaped curve as a function of energy where the relaxation time increases quite smoothly when $E = 0$ is approached, until it collapses to a minimum at the Dirac point. The spin precession time on the other hand stays approximately constant for the whole energy range. When the results are looked into more carefully, there are however quite big differences. The biggest difference is the magnitude of the spin relaxation time. In our calculations $\tau = 0.34$ ps at $E = 0$, a result which still agrees quite well. The maximum at 0.1 eV, where $\tau = 4.3$ ps, on the other hand is completely different from the $\tau = 0.8$ ps at 0.2 eV reported by van Tuan *et al.* Also, there is a slight kink at $E = 0$ in the spin precession time not present in their results.

The difference between the results is most likely explained by the different approximation of the delta function. In their supplementary material, the authors mention a thermal broadening of 0.027 eV. Even though this gives a relatively good approximation for the delta function, it is still way wider than the one used in our calculations, as seen in Figure 9b. The type of the broadening was not mentioned in the supplement and therefore both Lorenzian and Gaussian distributions are drawn to compare to our Chebyshev expansions with $N_m = 300$, 500, 1000. Even though the number of moments in each of the three cases is small compared to $N_m = 3000$ used in our other calculations, all of them feature a much sharper peak than either of the two distributions they are compared to.

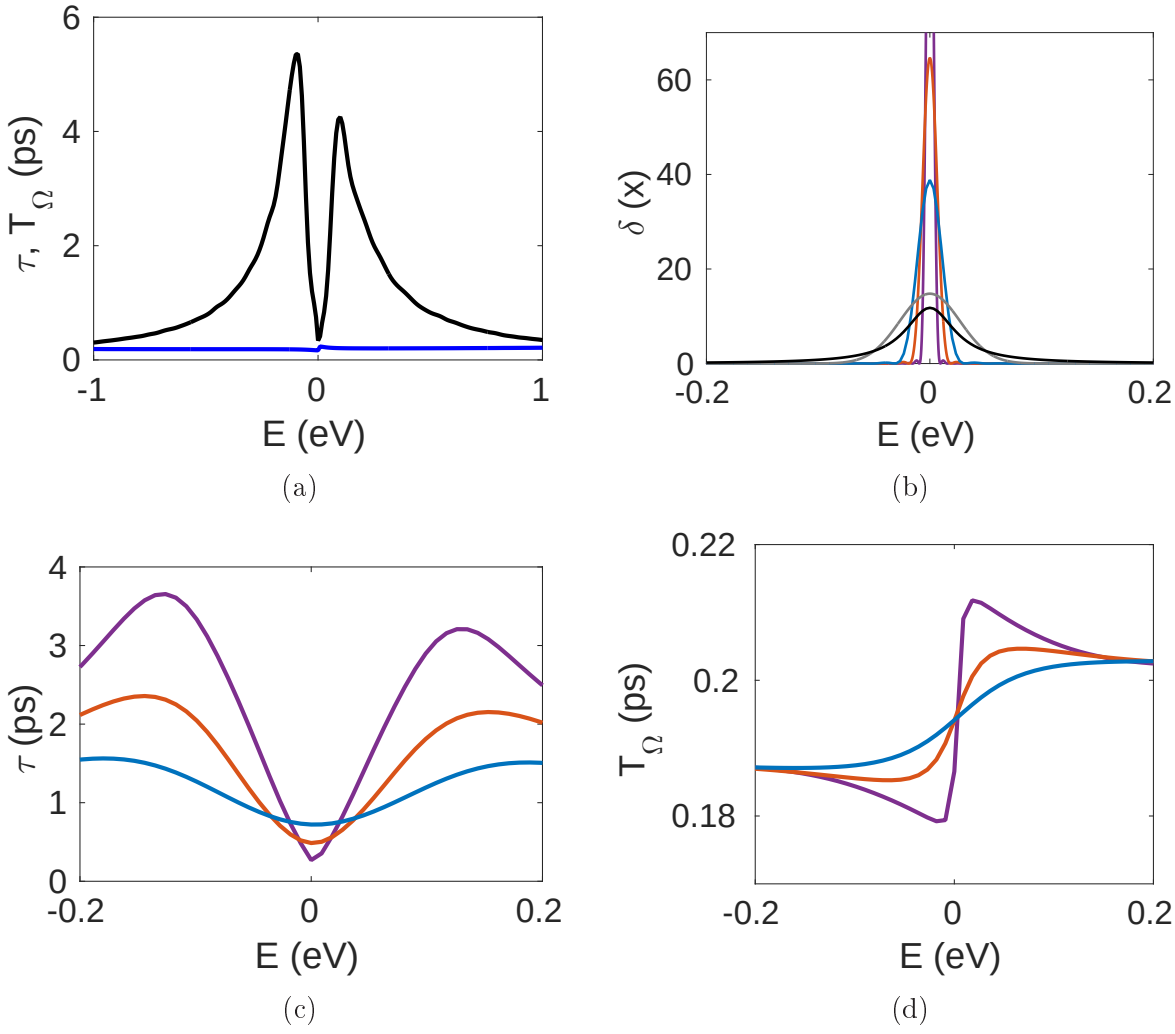


Figure 9: (a,c-d)Spin relaxation and precession times for 8% density of adatom plaquettes calculated with different amount of Chebyshev moments. (a) $N_m = 3000$ for both relaxation (black curve) and precession (blue). (b-d) The amount of moments are 300 for light blue, 500 for orange, and 1000 for purple. (b) Approximations to delta function with the different amount of moments. The black curve shows Lorenzian approximation with $\eta = 0.027$ eV while the gray one shows Gaussian with $\sigma = 0.027$ eV.

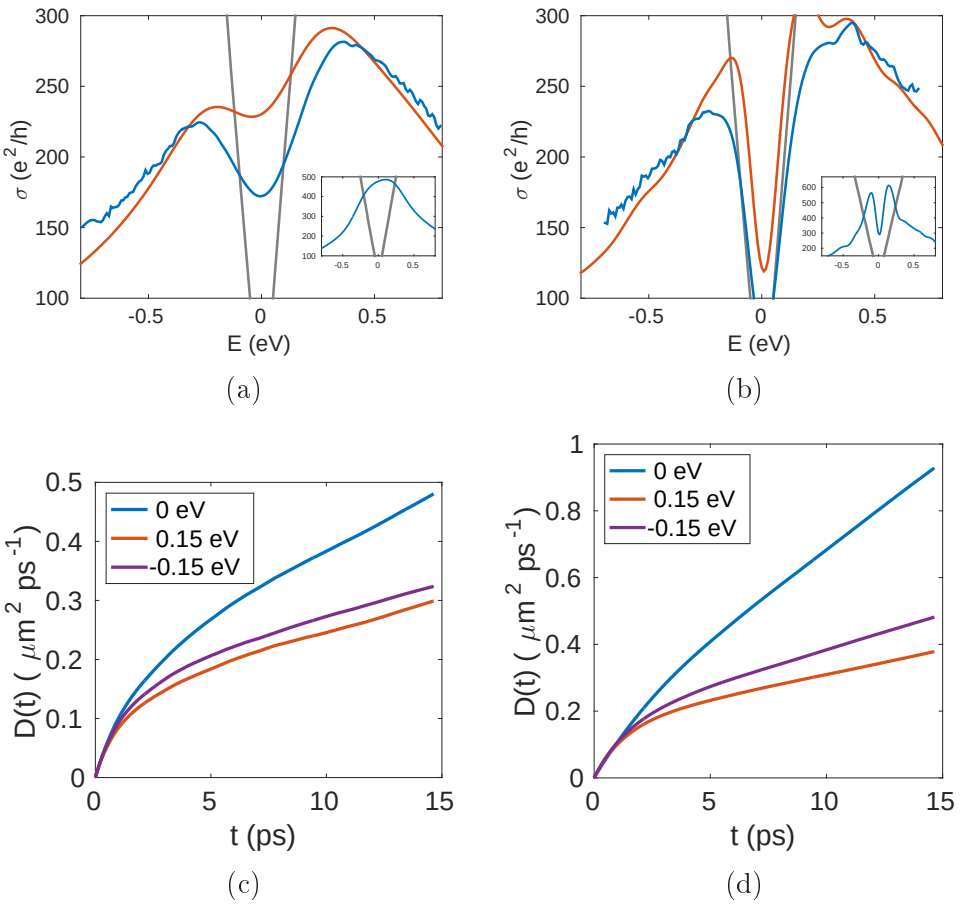


Figure 10: (a,b) Total conductivity for 8% concentration of adatom plaquettes measured at 1 $\mu m$ (blue), 5 ps (orange) and at 15 ps (inset) and pristine graphene at 1 $\mu m$ (gray curves). (c,d) Time-dependent diffusion coefficient at selected energies. Figures (a) and (c) are calculated with $N_m$=300 and (b) and (d) with $N_m$=1000.

The effect of $N_m$ is further investigated in Figures 9c and 9d, which show the spin relaxation and precession times calculated for the three cases considered in Figure 9b. As expected from the comparison between the delta function approximations, the case with fewest moments is closest to the results of van Tuan *et al.* The magnitude of $\tau$ is still too large across the whole energy range, but the shape is now fully consistent with their results. $T_\Omega$ on the other hand behaves now much more nicely as the kink at $E = 0$ has turned into a smooth bump. Because the approximations to the delta function are different, the results cannot be expected to be exactly the same, but they agree already quite well.

Another effect of the number of moments can be seen in the curious behaviour of conductivity near $E = 0$. During the first few picoseconds of the simulation, there is a minimum at zero in the conductivity, as seen in Figure 10. However, once time passes on enough, the depth of the minimum decreases and it actually becomes a maximum at long enough

times. This is caused by the increased broadening of states over time as the peak at 0.3 eV fills in the minimum. The incorrect behaviour is highlighted by comparing the magnitude of the conductivity to pristine graphene in the same figure. Pristine graphene should give an upper bound for conductivity for systems with defects with them and in our case we have multiple times bigger conductivity than that.

When the number of moments is increased, the correct behaviour is brought out. Figure 10b shows the conductivities at exact same times but with $N_m$=1000 instead of 300. This time the states do not get wider in energy and the minimum at zero also keeps its shape as time goes on. The results now also agree much better with the conductivity of pristine graphene. The pristine conductivity shown is calculated at constant length, and the corresponding plaquette conductivity agrees quite well with it. The results with constant time cannot be directly compared with the pristine case, but they also agree quite much better. They follow the behaviour from the pristine case much more closely and the bigger magnitude is fully explained by the different point of measurement.

There is still some discrepancy in our results compared to the ones by van Tuan et al. According to their calculations, the diffusion coefficient saturates at energies above 0.1 eV at 8% defect density. This was not the case in our results as $D(t)$ keeps on increasing for much wider range of energy. The magnitudes of the coefficient is quite close if our $N_m = 3000$ result is compared to theirs, but the behaviour is still a bit different. Either there is still some difference in the systems on microscopical level or the effect of the different approximations of the delta function is even higher.

## 5.5 Charge Puddles

### 5.5.1 Constant sized puddles

Both of the potential defects and adatom plaquettes considered earlier are very local defects and can result in sharp changes in the potential. Whereas this could be achieved by adatoms, too abrupt changes in potential are not likely to be present in real systems. A more realistic scenario would be a defect which spans over multiple sites and has smooth behaviour for the potential. In this section we particularly focus on Gaussian-shaped charge puddles, which are described as

$$U(r) = U_0^\sigma e^{-r^2/2r_0^2}, \tag{64}$$

where $U_0$ is the potential strength at the center of the puddle, located in the middle of some carbon hexagon, $r$ is the distance from the centre and $r_0$ is the width of the puddle. The potential strength is chosen separately for the spin channels but the center of the puddle is the same for both of them. These puddles could be caused for example by ripples in the graphene sheet or a magnetic substrate underneath the sample. The spin-dependency of the potential might stem from electron polarization of the puddle or ferromagnetic properties of the substrate. The numeric values used for the potentials are $U_0^\uparrow = 0.8$ eV and $U_0^\downarrow = 0.6$ eV. The defect angle is handled the same way it is done with the potential defects.

The potential strength decays to zero with these defects quite rapidly and to ease the forming of the Hamiltonian, a cutoff radius is introduced for each puddle. The cutoff is implemented such that only the sites inside a rectangular box centered at the defect site get finite values for the potential. The edges of the box are chosen such that the exponential coefficient, $e^{-r^2/2r_0^2}$ gets value 0.001 at the center of each side. Sites outside of this box will gain zero contribution from the particular defect. The puddles are allowed to overlap and the potential for a site is simply the sum over the contributions from all defects.

Because of their much larger nature, the amount of puddles we can place in the system is much smaller than that of the single-site potential defects. For example, a puddle with $r_0 = 10\ a_0$ covers an area which has roughly 240 atom sites. Therefore, 1% density of the potential defects would correspond to puddle density of 0.005%. However, the strength of the puddles gets much weaker near the edges of the puddles and the cases with equal coverages cannot be directly compared.

The behaviour of spin polarization with charge puddles depends greatly on whether the potential strength is kept constant for the puddles or is taken randomly from $[-U_0, U_0]$, as seen in Figure 11. When the potential is kept constant, dampened oscillation is still observed. This time, however, the behaviour is highly asymmetrical with respect to the Dirac point. On one side of the point the oscillation is much faster compared to the other one and the same side also dampens faster. The randomized potential on the other hand shows no signs of oscillation. The behaviour is completely symmetrical and the spin relaxation time is longer than on either side of the Dirac point in the constant case.

The differences between the two cases are mostly expected. The magnitude in the constant strength puddles is $U_0$, the endpoint of the potential interval from which the randomized strengths are taken. When the potential strength is randomized, the average magnitude of potential is lower than the value used in the constant case, causing the relaxation to take longer. The symmetry follows from the fact that the randomized potential is taken from -$U_0$ to $U_0$. Flipping the sign of the potential mirrors the results with respect to zero and when average is taken over the different potentials, there are equal amount of puddles with opposing signs, leading to the symmetric result. The most curious difference is the lack of oscillations in the randomized case. It seems that each puddle with different strength has its own energy-dependent oscillation frequency. When there are multiple different puddles in the same system, the competing frequencies suppress each other, leading to no oscillation in the end.

The behaviour of the conductivity for the charge puddles is different from either of the potential defects or adatom plaquettes, as seen in Fig. 11d. Just like the other defect types, $\sigma$ has a minimum at $E = 0$, but instead of staying constant or decaying at higher energies, this time $\sigma$ behaves quadratically near the zero energy. This is in a good agreement with scattering from charged impurities, for which the conductivity scales linearly as a function of charge carrier density $n$ [54]. Because $n$ depends quadratically on $E$, the conductivity scales as $E^2$ explaining our observation. On the other hand, the linear conductivity of the potential defects is explained by their much shorter range. Short range scatterers in

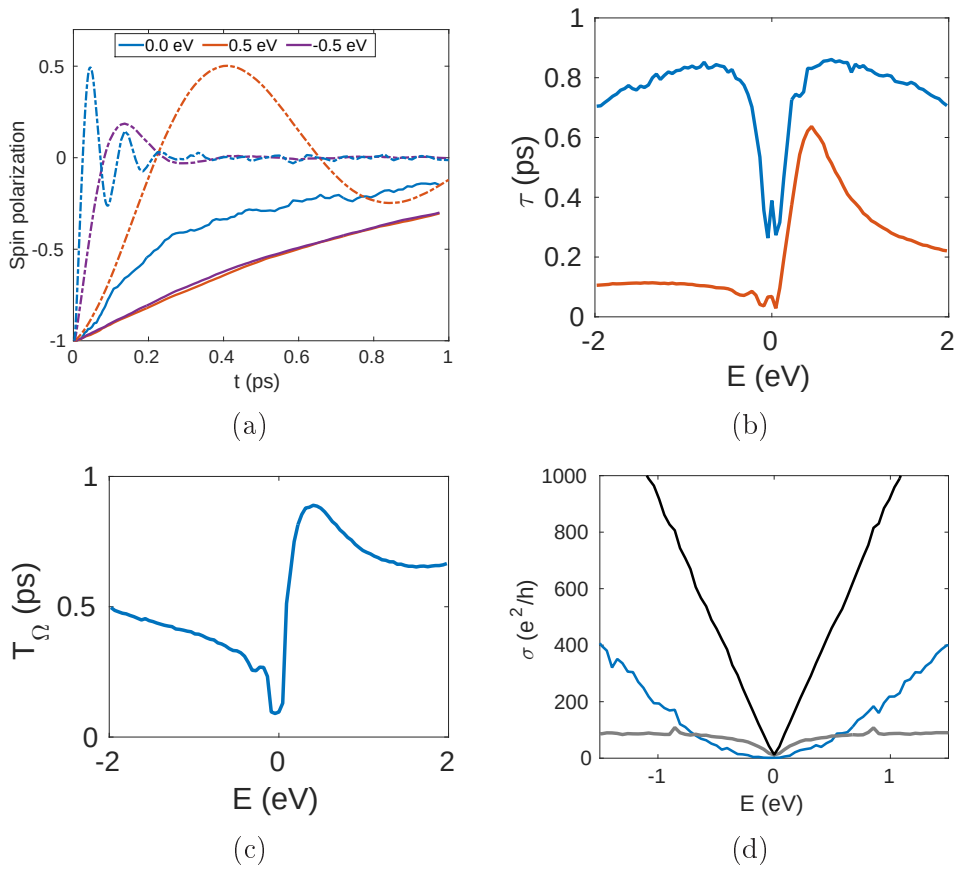


Figure 11: (a) Spin polarization as a function of time for three energies with $U_0^{\uparrow} = 0.8$ eV and $U_0^{\downarrow} = 0.6$ eV. The dashed lines feature constant potential while the solid lines have it randomized. (b) Spin relaxation time for randomized (blue) and contant (orange) potentials. (c) Spin precession time for the contant potential. (d) conductivity at $t = 0.6$ ps for randomized potential (blue) compared to pristine graphene (black) and potential defects (gray).

graphene have been shown to have constant conductivity [55] and is in agreement with our results.

### 5.5.2 Puddles with varying size

In real experiments, it is likely that the size of the puddles in the system is not uniform. In case the potential is caused by a substrate, it might have rough surface and affect the electron distribution unevenly. Therefore, it is good to also randomize the width of the puddles in addition to the potential strength. Having another parameter randomized causes the convergence to suffer slightly, but as seen from Figure 12, the results are still reasonably good even with the same number of random vectors in the calculation as before.

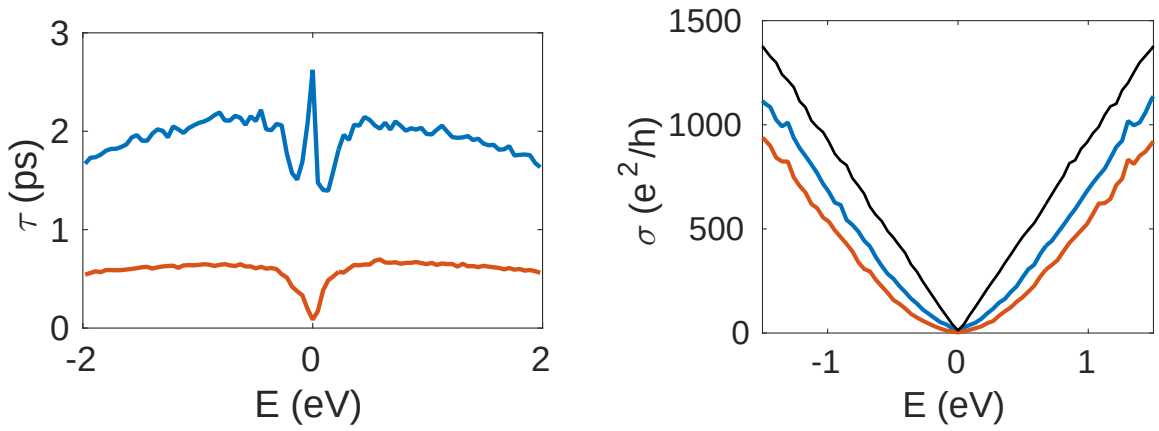


(a) (b)

Figure 12: (a) Time constant (b) Conductivity at $t = 0.6$ ps for puddles with randomized width. The blue curves correspond to maximum width of $10a_0$ and the orange ones to $15a_0$. The black line in (b) shows pristine graphene as a comparison.

The blue curve in Figure 12a shows the spin relaxation time when the puddle width is randomized uniformly between 0 and $10a_0$, while keeping the other parameters the same as before. With the exception of the vicinity of the zero energy, the behaviour is pretty much the same as before, with the time constant slowly decreasing with increasing energy. Near zero, the behaviour however changes drastically. Instead of dropping sharply and then forming a small peak at $E = 0$, the peak is now dominant and the drop in not nearly as sharp. The orange curve in the same figure shows the case where the randomization is taken over 0-$15a_0$. Again, the zero energy shows slightly different behaviour compared to the other cases, as there is a sharp drop and no peak at $E = 0$.

It seems that the peak at the zero energy is a feature originating from the smaller puddles in the system. The case with constant $r_0 = 10a_0$ was shown in Fig. 11b and it had only a small peak at $E = 0$. All of the puddles have smaller width than this in the randomization and the smaller puddles have to be responsible for the larger peak. In the system where randomization is taken from 0 to $15a_0$, it is basically guaranteed to have at least some puddles with $r_0 > 10a_0$ and it is enough to fade the peak away. It seems like the smaller puddles are too steep for the $E = 0$ charge carriers and since they cannot get into their range, the amount of spin flipping is reduced. Even a few larger puddles are enough to enable spin flipping near zero, as they have much gentler slope and allow the charge carriers to enter their area.

Outside of the zero-energy range, the results are quite expected. The spin relaxation times are a bit longer in the randomized case compared to the same non-randomized one. The randomization causes the average puddle size to be smaller and it is natural that it takes longer for the spin to relax. There is also not much going on with the conductivity. Both randomized cases feature the same parabolic energy dependence seen in the non-randomized

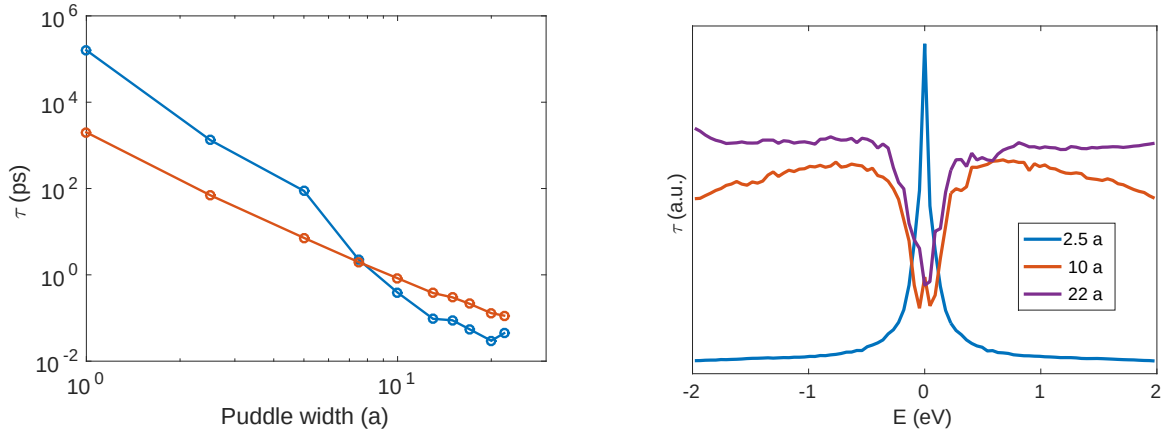


(a) (b)

Figure 13: (a) Spin relaxation time scaling as a function of puddle width. The two curves are measured at E=0 (blue) and E=1 eV (orange). (b) Behaviour of the relaxation time for different puddle widths. The curves have been scaled to fit into same figure and only the relative behaviour should be considered. All widths have unit of $a_0$, the C-C bond length in graphene.

case and the magnitude of the conductivity is not much smaller than in pristine graphene. With larger puddles the conductivity is a bit smaller as there is larger area scattering charge, but it seems that the puddles do not scatter charge significantly.

To further address the effect of the puddle size, the spin polarization was calculated with multiple constant puddle sizes. Figure 13a shows the behaviour of the time constant versus the puddle size. At $E = 1$ eV the behaviour is linear, suggesting a power law behaviour. At $E = 0$ there are straight portions, but overall the curve is not linear. This is mostly explained by the transition between the extremes seen in Figure 13b. In the small size limit the relaxation increases inversely to the energy as zero is approached, while the larger puddles have decreased relaxation near zero. Between these cases is a transition region, which was already seen earlier.

The behaviour of the relaxation time at $E = 1$ eV strongly suggests that there would be a power law scaling between it and the puddle width. To see if this is the case for all energies, a fitting to $ax^b$ was done across the calculated energy range. The fitting can be done in multiple ways and the results can be seen in Figure 14. Perhaps the easiest way of doing the fit is to take the logarithmic plot similar to Figure 13a and fit a straight line to the data. Alternatively, it is possible to get a fit directly for the power law by minimizing the squared sum of function $f(a,b) = \tau - ar_0^b$ across the puddle sizes $r_0$ and the corresponding spin relaxation times $\tau$. The third method utilizes the same minimization of squared sum, but instead of applying it directly to the data, the inverse of the relaxation time is taken.

The reason behind the three different ways of fitting is the different weights they give to

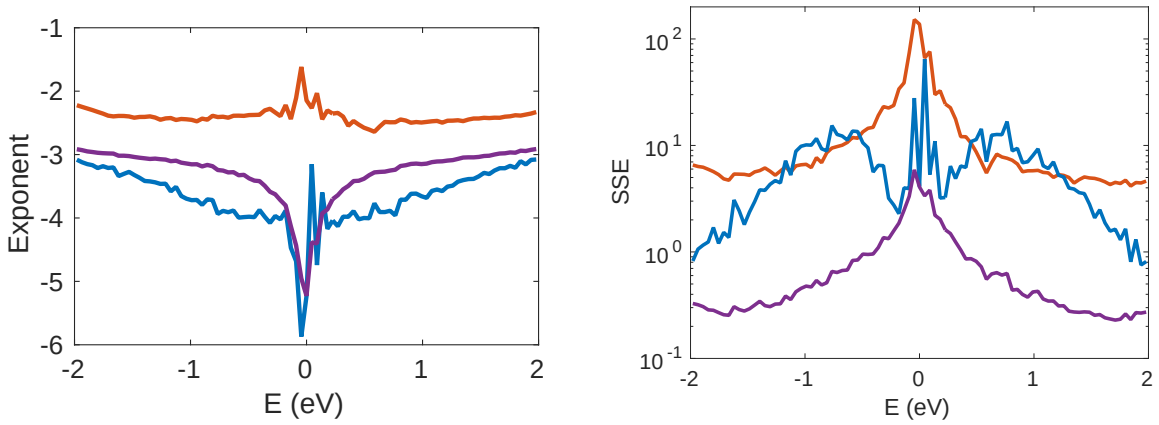


(a) (b)

Figure 14: (a) The exponent $b$ in the power law $ax^b$ fitting as a function of energy. (b) Sum of squared errors of the fits. Blue curve shows direct fit, the orange one fit to inverse relaxation time and the purple one a logarithmic fitting.

each data point. The fit to logarithmic plot gives roughly an equal weight for each point in the data, while the direct fits give more weight for their largest data points. For direct fit these are the smaller puddles, since they have longer relaxation time and for the inverse fit more weight is given to the larger puddles. To measure the goodness of each fit, a sum of squared error (SSE) was calculated between the fit and the actual data points. To ensure a fair comparison between the methods, the error was calculated on the logarithmic scale. On a regular linear scale there is way too much weight on the smallest puddles, since their relaxation time is few orders of magnitude larger compared to the larger ones.

The results given by the first two methods agree reasonably well with each other, as seen in Figure 14. The exponent in the power law mostly varies between -3 and -4 and at the zero energy it drops down even further. The zero-region however should not be taken too seriously, since the the transition mentioned earlier affects it the most. The third method gives considerably different results, as the exponent is roughly -2 with almost no energy dependence. The difference might be caused by the fluctuations that were present in the larger puddles. The inverse time fitting gives the most weight for the largest puddles and if they have inaccuracy in their values, so will the fit done by the third method.

The sum of squared error suggests that the first method would be the best of the three. It has the smallest error across the whole energy range and it also has the smoothest behaviour for the exponent. The method however benefits greatly from the way the SSE was calculated. Since the SSE is calculated in the logarithmic scale, it gives a natural advantage for the first method, since it already minimizes the SSE on the logarithmic scale in the linear fit. If the SSE was calculated on linear scale, the first method would have multiple orders of magnitude larger error because it doesn't give nearly as much weight for the smallest puddles. In any case, the first method seems to be the best in finding the

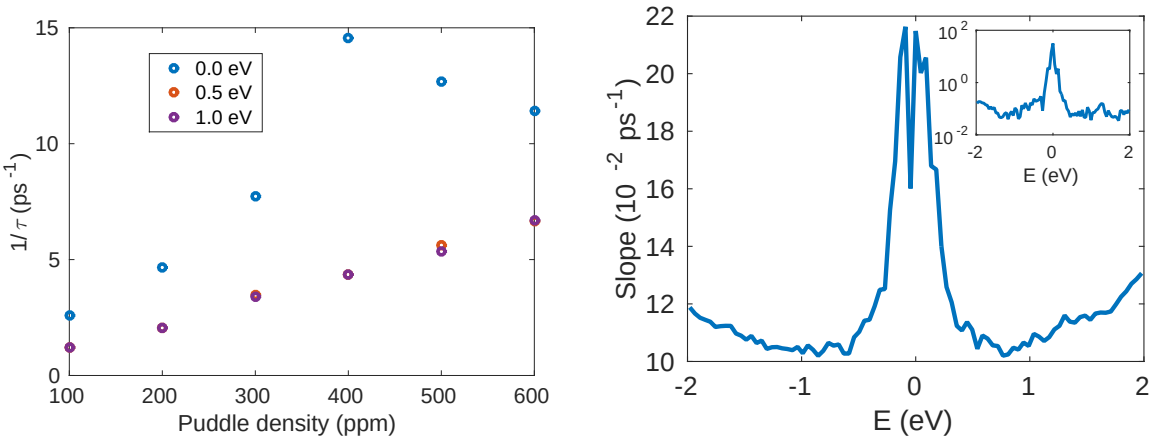


(a) (b)

Figure 15: (a) Scaling of the (inverse) relaxation time as a function of charge puddle density. (b) Slope of the linear fit as a function of energy. (inset) Sum of squared errors in the fit.

exponent correctly, even though the fit given by it might not be the best.

As a last result for the charge puddles, the scaling of the spin relaxation time was also calculated as a function of the puddle density. The results can be seen in Figure 15, where the inverse of the relaxation time is shown against the density. With the exception of the zero energy, the inverse seems to be scaling linearly with nearly constant slope across the energy. The transition observed with the previous results seems to be affected by the density, causing deviation from the linear behaviour for zero energy. As seen in the error, the fits are really good across the energy.

The linear scaling is a quite reasonable result. If the puddles do not interact with each other, each one will scatter spin with the same rate assuming the charge carriers traverse somewhat uniformly. Increasing the number of puddles would then increase the number of spin scattering events linearly. The relaxation time is inversely proportional to the number of spin scattering events, which means that the inverse also increases linearly. In high enough concentrations the puddles start to overlap and interact with each other, but at least in the range that was calculated, this was not yet the case.

## 5.6 Charge carrier density evolution

In the absence of a good measure for spin flipping conductivity the spin polarization has been so far the best way to describe the spin behaviour. While it gives useful information about the system, it doesn't address the transport properties as well as conductivity or conductance would. One alternative way of looking into the transport properties is to calculate the time-evolution of the wave function and see how the charge density evolves in time. An especially interesting case is localized initial state, since it gives a way to measure

distance travelled by the wave packet.

There are some technical problems when the density is calculated, especially considering the amount of data that is acquired in the computation. The system we have calculated so far have had roughly million atoms in them. It takes roughly 16MB of memory to store the density for one state vector using double precision numbers, as each atom has separate densities for both spins. Time evolution requires roughly 100 steps to calculate the density accurately enough for relevant time scales, which means the amount of memory required to store the evolution of one random state is in the order of gigabytes. Accurate calculations require tens of random vectors and the amount of storage required becomes too large to handle.

The memory usage can be reduced by averaging the density over a few sites. For example we can calculate the density over a grid of 10x10 squares, reducing the required memory by a factor of 100. This kind of box filter is a basic operation on a GPU and it performs really efficiently. The averaging process decreases the accuracy in location slightly, but in small enough areas this does not matter.

So far most of the quantities have been calculated as a function of energy. When density is considered, the energy is not as important and it can be dropped out of the calculations, saving both computational time and size of the output. Physically the most relevant energy range is the vicinity of the Dirac point and to focus the results to this area, the initial state can be manipulated with imaginary time evolution. When operator $e^{-\tau \hat{H}^2}$ is applied to the state, the energy eigenstates are weighted with an exponential coefficient $e^{-\tau E^2}$. After renormalization, the higher energies vanish from the state and the relevant energy range is left in. An illustration of how the DOS changes is shown in Figure 16a.

The initial shape of the wave packet was chosen to be Gaussian, similar to how the charge puddles were defined. The width of the packet was chosen to be 5 $a_0$ and it was normalized to the number of atoms in the system. The initial state might be slightly unphysical, since it corresponds to scenario where every electron of the system is in the same location, but the dynamics given by it should come out correctly nevertheless as the interaction effects are neglected. An example of the time evolution in the presence of charge puddles can be seen in Figure 16b. The spreading happens quite fast and in the last snapshot, which is taken at $t = 48$ fs, the width of the packet is already 10 nm. The hexagonal shape of the spreading packet is caused by the graphene lattice and the lack of excessive scattering in the system. The strength of the puddles is weak enough that the initial symmetry of the packet is retained, unlike in the presence of stronger defects in higher density. For example the potential defects with strength of $\pm 2$ eV and 8% density cause the packet to become circular after the first 60 fs of the simulation. With the puddles, the hexagonal shape is retained for the whole 2 ps of the simulation.

The Figure 16b also shows how similar the spins behave. The shape and size of the packet are identical as time passes on and the only difference is the amount of each spin. Also, the ratio between the spins stays quite uniform across the system in the presence of charge puddles as seen in Figure 17. When the average spin percentages are compared, their

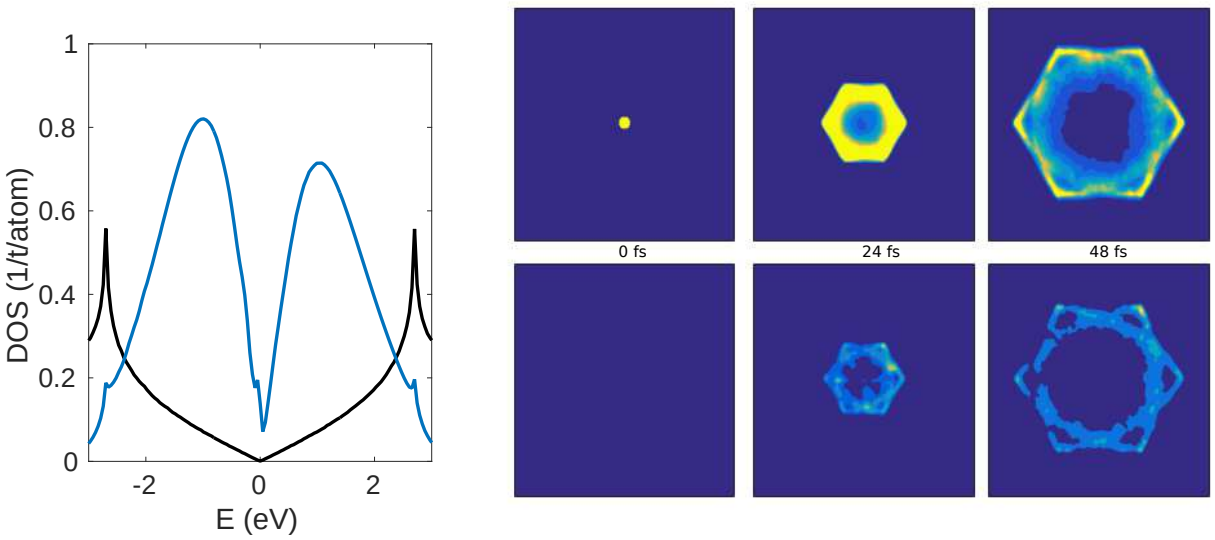


(a) (b)

Figure 16: (a) The density of states after imaginary time evolution (blue) compared to regular DOS (black) (b) Time evolution of the density of Gaussian shaped initial state in the presence of charge puddles. The first line shows up-spin and the second one down-spin. The snapshots are taken from $t = 0$, 24 and 48 fs.

overall behaviour does not differ much from the local ones, especially in the later parts of the simulation. After the first 0.1 ps of the simulation, both local and global values are practically the same and most of the interesting phenomena occur before that time. Up until 0.05 ps, the density behaves smoothly for all of the points of measurement. After that, the percentage of the up spin drops fast with a strong dependence on the distance from the center. For the closest points, the percentage starts to drop immediately, while for the further points it takes much longer to drop down.

The times at which the drops occur roughly correspond to the moments at which the main wave packet passes the points of measurement. At t=0.05 ps the widest part of the packet has travelled 5.7 nm from the centre and at 0.1 ps the narrowest part has just passed the 9 nm distance, at which the furthest measurement was done. Because of its hexagonal symmetry, the wave packet reaches the same lengths at slightly different times, making the passing a little longer event. The sudden drop in the percentage of up spin when the main packet passes by suggests that there is a rather strong correlation between the scattering of charge and spin. The first parts of the wave packet that reach the points of measurement are the fastest, which means they cannot have had many scattering events on their way. The percentage of up spin in these parts is also larger than on average, which means they also have had less spin scattering. The most of the down spin is carried by the main packet and as it passes the point of measurement, the down density increases drastically. At the 0.1 ps mark the wave packet has almost reached the whole system and after that, the behaviour follows the average closely, as the density has more or less reached the equilibrium.

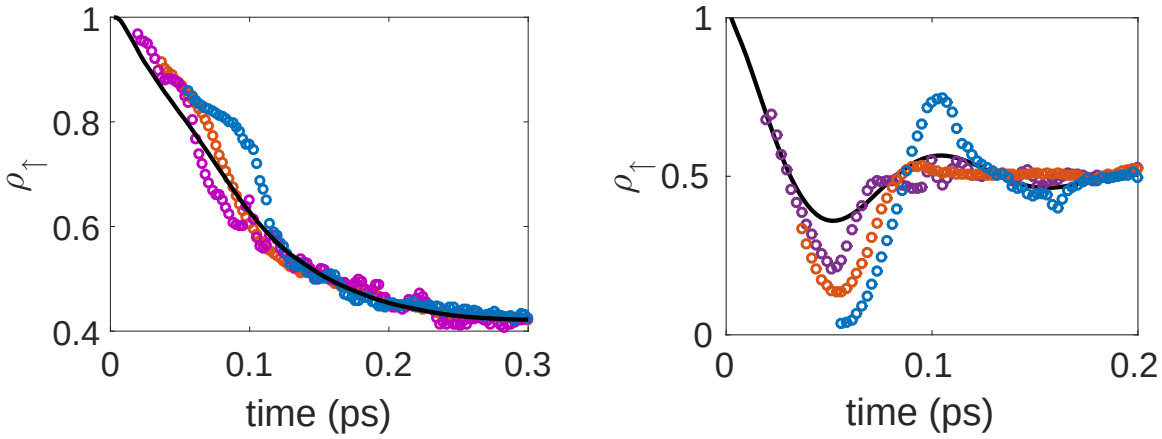


(a) (b)

Figure 17: Percentage of up spin density as a function of time at distances of 4.5 nm (purple), 6.2 nm (orange) and 9.2 nm (blue) compared to the overall density of up spin (black). (a) shows the results for charge puddles and (b) for potential defects. The data sets start from the moment when density becomes large enough that it can be numerically distinguished from zero.

The potential defects are much stronger scatterers and therefore their local spin behaviour differs quite much from the global one. First of all, the wave packet spreads a lot slower, as seen from the later starting point of the data sets in Figure 17b. There is now a really strong dependence on the point at which the measurement is made. The amplitude of the spin oscillation decays much slower in the farther points and they also oscillate slightly slower. This time the wave packet reaches the whole system at t=0.12 ps, but there is still some difference between the local and global behaviours. It would seem that the stronger potential defects keep the different parts of the system much more separated, allowing there to be different behaviour at different locations.

The different behaviour of spin is especially well seen in the profiles of up spin percentage shown in Figure 18. With charge puddles in the system, there are two levels of percentages, one closer to the center and one further away. The closer one has slightly less percentage of up spin and between the two levels there is rather steep rise. The rise is most likely caused by the main wave packet passing the radius, as their locations match. The spin profile stays quite uniform across time, unlike with the potential defects, for which the profile changes in shape a lot as time passes. In principle the behaviour is more or less similar to the puddles as there is again two levels and a slope between them. This time however the further level can get any values depending on time. It seems that, unlike with the charge puddles, there is no coupling between the spin and charge scattering as this time the faster electrons undergo spin scattering.

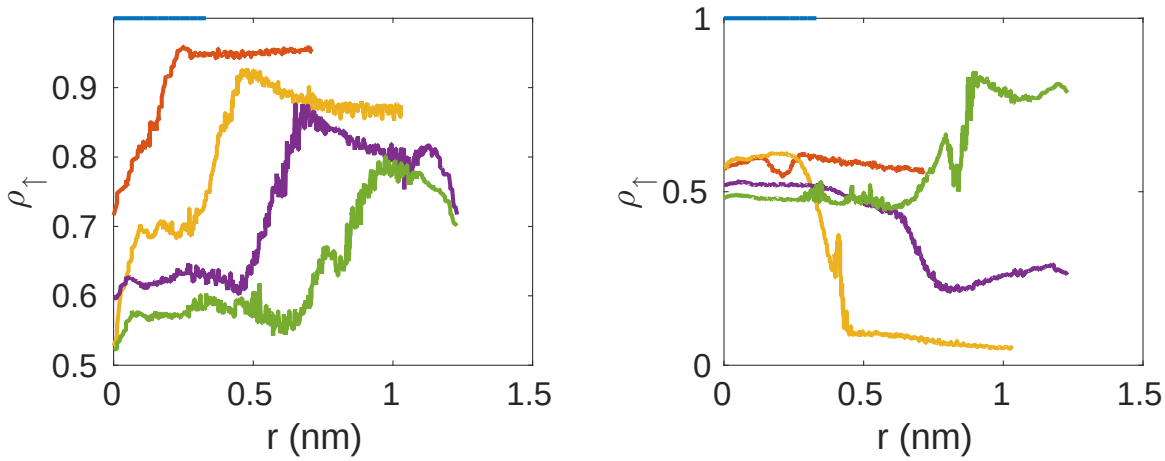


(a) (b)

Figure 18: Percentage of up spin as a function of distance from the center. The curves are for t= 0, 0.02, 0.05, 0.08 and 0.1 ps, for blue, orange, yellow, purple and green, respectively. Figure (a) is for charge puddles and (b) for 1% potential defects.

# 6 Conclusions

Spin-dependent transport properties of electrons in graphene were studied in this thesis. The research was done using the real-space Kubo-Greenwood formalism, implemented on graphics processing units. A spin-dependent formulation was derived starting from Kubo conductivity and an implementation was created on top of an existing spinless code. The implementation was finally tested on various types of defects embedded in graphene.

It turned out that the concept of spin-flipping conductivity is somewhat ill-defined. While it can be defined in the Kubo-Greenwood formalism, this definition does not capture all spin flipping effects in the system, and in particular the effect of spin-dependent potential is completely left out. This obviously does not agree with the Landauer-Büttiker formalism, for which flipping conductance can be defined. The difference comes from the different perspectives to the transport: in the Landauer-Büttiker formalism the conductance is accessed through transmittance and is more or less related to electric current, while Kubo-Greenwood focuses more on the density evolution which is more related to the movement of separate electrons. Within the microscopic view of Kubo-Greenwood formalism, it seems that spin polarization provides a better measure to describe spin flipping.

In the ribbon geometry the results between Landauer-Büttiker and Kubo-Greenwood agree surprisingly well considering the completely different approaches. The spin-conserving conductances are practically equal considering the numerical errors in the Kubo-Greenwood calculation and the slightly different systems. The spin flipping behaviour also seems to be similar in both formalisms, even though they measure it by different means. The defects are active at same energies, which strongly suggests that both formalisms capture the same

effects, albeit in a different way. This is even more highlighted when the defects are placed on the edges of the system, as they are much more active when placed there.

The comparison between the two methods was limited to the ribbon geometry since Landauer-Büttiker cannot handle wider systems nearly as efficiently. Kubo-Greenwood on the other hand has excellent performance in wider systems. Even though the spin-part of the implementation was not optimized for performance, the execution times of the code were short enough that it was sensible to calculate enough random vectors and have the results converge. The convergence depends on the system and in general the more defects there are in the system, the fewer vectors are required for convergence.

Another important factor in the calculation is the number of moments used in the Chebyshev expansion. Fewer moments allow smoother results and faster convergence. This however comes at the expense of loss of energy resolution. Fewer moments mean that the approximation of delta function becomes worse and the states are spread to wider range of energy. As seen with the adatom plaquettes, the spreading causes much smoother behaviour for peaked quantities and may result in large errors. In general, the number of moments should be chosen as high as possible while keeping the computational time reasonable.

Out of three defect types studied, the local potential defects are quite pure mathematical defects, since it would be really hard to get potential with 2 eV strength on a single site without altering the neighbouring sites. The adatom plaquettes on the other hand are from the other end of the spectrum and are perhaps the closest of the three to model real world defects. The charge puddles lie between the other two, as they have been observed experimentally, but it is not known if the potential can be spin-dependent or not. From these three defect types, the puddles provided the most interesting features at the studied parameter ranges. Even though the used potential strength for the puddles is relatively strong at 0.7 eV, they don't scatter charge too much as seen from its conductivity compared to pristine graphene.

The puddles also feature an interesting transition in the behaviour of the zero energy range. In the limit of large puddles, the zero energy has the fastest spin relaxation. As the puddle width is decreased, the relaxation time increases faster for the zero energy and eventually higher energies relax the fastest. The transition is most likely caused by the profile of the puddles. For larger puddles the potential rises over long distance and even zero energy modes are allowed to enter their area. When the width gets smaller, their slope gets steeper and steeper, eventually blocking the entrance to the puddles.

All in all, the implementation proved to be effective in studying the spin-dependent properties of graphene. The method should be easily extendable to all materials and defects that can be modelled with tight binding. It is slightly disappointing that the formalism cannot handle spin-flipping conductivity but spin polarization covers this weakness quite well. The results for the spin polarization with the charge puddles suggest that long-range scatterers affect spin much more effectively than they do charge. This might explain the short spin lifetimes observed in the experiments even on high-quality samples [11, 56], if the samples in the experiments have defects similar to the studied charge puddles.

# 7 References


[1] C. Chappert, A. Fert, and F. N. van Dau, "The emergence of spin electronics in data storage," *Nat. Mater*, vol. 6, pp. 813–823, 2007.

[2] H. Ohno, F. Matsukura, and Y. Ohno, "Semiconductor spin electronics," *JSAPI*, pp. 4–13, 2002.

[3] S. A. Wolf, D. D. Awschalom, R. A. Buhrman, J. M. Daughton, S. von Molnar, M. L. Roukes, A. Y. Chtchelkanova, and D. M. Treger, "Spintronics: A spin-based electronics vision for the future," *Science*, vol. 294, pp. 1488–1495, 2001.

[4] S. D. Bader and S. S. P. Parkin, "Spintronics," *Ann. Rev. Condens. Phys.*, vol. 1, pp. 71–88, 2010.

[5] O. V. Yazyev and L. Helm, "Defect-induced magnetism in graphene," *Phys. Rev. B*, vol. 75, p. 125408, 2007.

[6] J. O. Sofo, G. Usaj, P. S. Cornaglia, A. M. Suarez, A. D. Hernández-Nieves, and C. A. Balseiro, "Magnetic structure of hydrogen-induced defects on graphene," *Phys. Rev. B*, vol. 85, p. 115405, 2012.

[7] X. Hong, S.-H. Cheng, C. Herding, and J. Zhu, "Colossal negative magnetoresistance in dilute fluorinated graphene," *Phys. Rev. B*, vol. 83, p. 085410, 2011.

[8] S. Kattel, P. Atanassov, and B. Kiefer, "Stability, electronic and magnetic properties of in-plane defects in graphene: A first-principles study," *J. Phys. Chem. C*, vol. 116, pp. 8161–8166, 2012.

[9] M. Gmitra, S. Konschuh, C. Ertler, C. Ambrosch-Draxl, and J. Fabian, "Band-structure topologies of graphene: Spin-orbit coupling effects from first principles," *Phys. Rev. B*, vol. 80, p. 235431, 2009.

[10] S. Konschuh, M. Gmitra, and J. Fabian, "Tight-binding theory of the spin-orbit coupling in graphene," *Phys. Rev. B*, vol. 82, p. 245412, 2010.

[11] W. Han, R. K. Kawakami, M. Gmitra, and J. Fabian, "Graphene spintronics," *Nature Nanotech.*, vol. 9, pp. 794–807, 2014.

[12] P. Seneor, B. Dlubak, M.-B. Martin, A. Anane, H. Jaffres, and A. Fert, "Spintronics with graphene," *MRS Bull.*, vol. 37, pp. 1245–1254, 2012.

[13] R. Kubo, "Statistical-mechanical theory of irreversible processes. I. general theory and simple applications to magnetic and conduction problems," *J. Phys. Soc. Jpn.*, vol. 12, pp. 570–586, 1957.

[14] D. A. Greenwood, "The Boltzmann equation in the theory of electrical conduction in metals," *Proc. Phys. Soc.*, vol. 71, p. 585, 1958.

[15] S. Datta, *Electronic transport in mesoscopic systems*. Cambridge University Press, 1995.

[16] P. R. Wallace, "The band theory of graphite," *Phys. Rev.*, vol. 71, pp. 622–634, 1947.

[17] S. Reich, J. Maultzsch, C. Thomsen, and P. Ordejón, "Tight-binding description of graphene," *Phys. Rev. B*, vol. 66, p. 035412, 2002.

[18] M. R. Thomsen, M. M. Ervasti, A. Harju, and T. G. Pedersen, "Spin relaxation in hydrogenated graphene," *Phys. Rev. B*, vol. 92, p. 195408, 2015.

[19] V. Vierimaa, "Spin-dependent transport of graphene nanoribbons," *Special assignment*, Aalto University, 2015.

[20] J. Zhou, Q. Wang, Q. Sun, X. S. Chen, Y. Kawazoe, and P. Jena, "Ferromagnetism in semihydrogenated graphene sheet," *Nano Lett.*, vol. 9, pp. 3867–3870, 2009.

[21] R. Singh and P. Kroll, "Magnetism in graphene due to single-atom defects: dependence on the concentration and packing geometry of defects," *J. Phys. Condens. Matter*, vol. 21, p. 196002, 2009.

[22] A. Harju, T. Siro, F. F. Canova, S. Hakala, and T. Rantalaiho, *Applied Parallel and Scientific Computing: 11th International Conference, PARA 2012, Helsinki, Finland, June 10-13, 2012, Revised Selected Papers*, ch. Computational Physics on Graphics Processing Units, pp. 3–26. Berlin, Heidelberg: Springer Berlin Heidelberg, 2013.

[23] J. D. Owens, M. Houston, D. Luebke, S. Green, J. E. Stone, and J. C. Phillips, "GPU computing," *Proceedings of the IEEE*, vol. 96, pp. 879–899, 2008.

[24] V. W. Lee, C. Kim, J. Chhugani, M. Deisher, D. Kim, A. D. Nguyen, N. Satish, M. Smelyanskiy, S. Chennupaty, P. Hammarlund, R. Singhal, and P. Dubey, "Debunking the 100x GPU vs. CPU myth: An evaluation of throughput computing on CPU and GPU," *SIGARCH Comput. Archit. News*, vol. 38, pp. 451–460, 2010.

[25] M. Harris, "Mapping computational concepts to GPUs," in *ACM SIGGRAPH 2005 Courses*, SIGGRAPH '05, (New York, NY, USA), ACM, 2005.

[26] M. Bauer, H. Cook, and B. Khailany, "Cudadma: Optimizing GPU memory bandwidth via warp specialization," in *Proceedings of 2011 International Conference for High Performance Computing, Networking, Storage and Analysis*, SC '11, (New York, NY, USA), pp. 12:1–12:11, ACM, 2011.

[27] R. Vuduc, A. Chandramowlishwaran, J. W. Choi, M. E. Guney, and A. Shringarpure, "On the limits of GPU acceleration," in *Proc. USENIX Wkshp. Hot Topics in Parallelism (HotPar)*, (Berkeley, CA, USA), 2010.

[28] S. Hong and H. Kim, "An analytical model for a GPU architecture with memory-level and thread-level parallelism awareness," *SIGARCH Comput. Archit. News*, vol. 37, pp. 152–163, 2009.

[29] Fan, Z. and Uppstu, A., and Siro, T. and Harju, A., "Efficient linear-scaling quantum transport calculations on graphics processing units and applications on electron transport in graphene," *Comput. Phys. Commun.*, vol. 185, pp. 28–39, 2014.

[30] Nvidia, "CUDA toolkit manual v7.5." `http://docs.nvidia.com/cuda/index.html`, 2016.

[31] A. Lherbier, S. M.-M. Dubois, X. Declerck, Y.-M. Niquet, S. Roche, and J.-C. Charlier, "Transport properties of graphene containing structural defects," *Phys. Rev. B*, vol. 86, p. 075402, 2012.

[32] Y. Hancock, A. Uppstu, K. Saloriutta, A. Harju, and M. J. Puska, "Generalized tight-binding transport model for graphene nanoribbon-based systems," *Phys. Rev. B*, vol. 81, p. 245402, 2010.

[33] M. M. Ervasti, Z. Fan, A. Uppstu, A. V. Krasheninnikov, and A. Harju, "Silicon and silicon-nitrogen impurities in graphene: Structure, energetics, and effects on electronic transport," *Phys. Rev. B*, vol. 92, p. 235412, 2015.

[34] M. Büttiker, Y. Imry, R. Landauer, and S. Pinhas, "Generalized many-channel conductance formula with application to small rings," *Phys. Rev. B*, vol. 31, pp. 6207–6215, 1985.

[35] L. E. F. Torres, S. Roche, and J.-C. Charlier, *Introduction to Graphene-Based Nanomaterials: From Electronic Structure to Quantum Transport.* Cambridge University Press, 2014.

[36] S. Datta, *Lessons from Nanoelectronics: A New Perspective on Transport.* World Scientific, 2012.

[37] C. H. Lewenkopf and E. R. Mucciolo, "The recursive green's function method for graphene," *J. Comput. Electron.*, vol. 12, pp. 203–231, 2013.

[38] M. H. Lee, "Fick's law, Green-Kubo formula, and Heisenberg's equation of motion," *Phys. Rev. Lett.*, vol. 85, pp. 2422–2425, 2000.

[39] T. P. Pareek and P. Bruno, "Spin coherence in a two-dimensional electron gas with rashba spin-orbit interaction," *Phys. Rev. B*, vol. 65, p. 241305, 2002.

[40] M. Urech, V. Korenivski, N. Poli, and D. B. Haviland, "Direct demonstration of decoupling of spin and charge currents in nanostructures," *Nano Lett.*, vol. 6, pp. 871–874, 2006.

[41] A. Weiße, G. Wellein, A. Alvermann, and H. Fehske, "The kernel polynomial method," *Rev. Mod. Phys.*, vol. 78, pp. 275–306, 2006.

[42] Z. Fan, T. Siro, and A. Harju, "Accelerated molecular dynamics force evaluation on graphics processing units for thermal conductivity calculations," *Comput. Phys. Commun.*, vol. 184, pp. 1414 – 1425, 2013.

[43] T. Siro and A. Harju, "Exact diagonalization of the Hubbard model on graphics processing units," *Comput. Phys. Commun.*, vol. 183, pp. 1884 – 1889, 2012.

[44] "Intel product specifications." `http://ark.intel.com`, Accessed 21.1.2016.

[45] N. M. R. Peres, A. H. Castro Neto, and F. Guinea, "Conductance quantization in mesoscopic graphene," *Phys. Rev. B*, vol. 73, p. 195411, 2006.

[46] D. van Tuan, F. Ortmann, D. Soriano, S. O. Valenzuela, and S. Roche, "Pseudospin-driven spin relaxation mechanism in graphene," *Nature Phys.*, vol. 10, pp. 857–863, 2014.

[47] Y.-T. Zhang, Z.-F. Song, and Y.-C. Li, "Electron spin precession in two-dimensional electron gas with Rashba spin–orbit coupling," *Phys. Lett. A*, vol. 373, pp. 144 – 147, 2008.

[48] P. Boross, B. Dora, A. Kiss, and F. Simon, "A unified theory of spin-relaxation due to spin-orbit coupling in metals and semiconductors," *Sci. Rep.*, vol. 3, 2013.

[49] H. Ochoa, A. H. Castro Neto, and F. Guinea, "Elliot-Yafet mechanism in graphene," *Phys. Rev. Lett.*, vol. 108, p. 206808, 2012.

[50] M. I. Dyakonov and V. I. Perel, "Spin relaxation of conduction electrons in noncentrosymmetric semiconductors," *Sov. Phys. - Solid State*, vol. 13, pp. 3023–3026, 1972.

[51] D. Huertas-Hernando, F. Guinea, and A. Brataas, "Spin-orbit-mediated spin relaxation in graphene," *Phys. Rev. Lett.*, vol. 103, p. 146801, 2009.

[52] D. Marchenko, A. Varykhalov, M. Scholz, G. Bihlmayer, E. Rashba, A. Rybkin, A. Shikin, and O. Rader, "Giant rashba splitting in graphene due to hybridization with gold," *Nat. Commun.*, vol. 3, 2012.

[53] C. Weeks, J. Hu, J. Alicea, M. Franz, and R. Wu, "Engineering a robust quantum spin hall state in graphene via adatom deposition," *Phys. Rev. X*, vol. 1, p. 021001, 2011.

[54] S. Adam, E. H. Hwang, V. M. Galitski, and S. Das Sarma, "A self-consistent theory of graphene transport," *PNAS*, vol. 104, pp. 18392–18397, 2007.

[55] T. Ando, "Screening effect and impurity scattering in monolayer grpahene," *J. Phys. Soc. Jpn*, vol. 75, p. 074716, 2006.

[56] M. H. D. Guimarães, A. Veligura, P. J. Zomer, T. Maassen, I. J. Vera-Marun, N. Tombros, and B. J. van Wees, "Spin transport in high-quality suspended graphene devices," *Nano Lett.*, vol. 12, pp. 3512–3517, 2012.